Chemical exchange saturation transfer (CEST) and MR *Z*-spectroscopy *in vivo*: a review of theoretical approaches and methods

TOPICAL REVIEW

Chemical exchange saturation transfer (CEST) and MR *Z*-spectroscopy *in vivo*: a review of theoretical approaches and methods

Moritz Zaiss[1] **and Peter Bachert**

Department of Medical Physics in Radiology, Deutsches Krebsforschungszentrum (DKFZ), Im Neuenheimer Feld 280, D-69120 Heidelberg, Germany

E-mail: m.zaiss@dkfz-heidelberg.de

Abstract
Chemical exchange saturation transfer (CEST) of metabolite protons that undergo exchange processes with the abundant water pool enables a specific contrast for magnetic resonance imaging (MRI). The CEST image contrast depends on physical and physiological parameters that characterize the microenvironment such as temperature, pH, and metabolite concentration. However, CEST imaging *in vivo* is a complex technique because of interferences with direct water saturation (spillover effect), the involvement of other exchanging pools, in particular macromolecular systems (magnetization transfer, MT), and nuclear Overhauser effects (NOEs). Moreover, there is a strong dependence of the diverse effects on the employed parameters of radiofrequency irradiation for selective saturation which makes interpretation of acquired signals difficult. This review considers analytical solutions of the Bloch–McConnell (BM) equation system which enable deep insight and theoretical description of CEST and the equivalent off-resonant spinlock (SL) experiments. We derive and discuss proposed theoretical treatments in detail to understand the influence of saturation parameters on the acquired *Z*-spectrum and how the different effects interfere and can be isolated in MR *Z*-spectroscopy. Finally, we provide an overview of reported CEST effects *in vivo* and discuss proposed methods and technical approaches applicable to *in vivo* CEST studies on clinical MRI systems.

(Some figures may appear in colour only in the online journal)

---

[1] Author to whom any correspondence should be addressed.

Contents

List of abbreviations

α	labeling efficiency
APT	amide proton transfer
APEX	amine proton exchange
B_0	induction of the static magnetic field
$B_1(t)$	oscillating rf field
BM	Bloch–McConnell
BS	Bloch–Solomon
CERT	chemical exchange rotation transfer
CEST	chemical exchange saturation transfer
cw	continuous wave
DCE-MRI	dynamic contrast-enhanced MRI
δ	chemical shift (ppm)
$\delta\omega$	difference in Larmor frequency (rad s^{-1})
$\Delta\omega$	frequency offset (rad s^{-1})
f_b	relative population fraction ($f_b = M_{0,b}/M_{0,a}$)
FLEX	frequency-labeled exchange

FS	full-saturation or full-saturation limit
FWHM	full width at half maximum
γ	gyromagnetic ratio
GAG	glycosaminoglycan
k_a	backward exchange rate (from pool a to pool b) ($k_a = f_b k_b$)
k_b	forward exchange rate (from pool b to pool a)
LS	large-shift or large-shift limit
M_0	thermal equilibrium magnetization
$M_{0,a}$	thermal equilibrium magnetization of pool a (water pool)
$M_{0,b}$	thermal equilibrium magnetization of pool b (dilute solute pool)
M_i	initial magnetization
M_{sat}	magnetization after saturation
MRI	magnetic resonance imaging
MRS	*in vivo* NMR spectroscopy
MRZS	MR Z-spectroscopy
MT	magnetization transfer
MTC	magnetization transfer contrast
MTR	magnetization transfer ratio
NMR	nuclear magnetic resonance
NOE	nuclear Overhauser effect (of dipolar-coupled nuclear spin systems in liquids)
ω_0	Larmor frequency ($\omega_0 = \gamma B_0$)
ω_1	Rabi frequency given by the amplitude of the rf field ($\omega_1 = \gamma B_1$)
ω_{eff}	Rabi frequency given by the amplitude of the effective field ($\omega_{eff} = \gamma B_{eff}$)
PT	polarization transfer
PTR	proton transfer Ratio
P_z	projection factor on z-axis of the rotating frame
$P_{z\,eff}$	projection factor on z-axis of the effective frame
R_1	longitudinal relaxation rate ($R_1 = 1/T_1$)
R_2	transversal relaxation rate ($R_2 = 1/T_2$)
$R_{1\rho}$	longitudinal relaxation rate in the rotating frame ($R_{1\rho} = 1/T_{1\rho}$)
R_{eff}	longitudinal relaxation rate in the effective frame ($R_{1\rho}$ of water exclusively)
R_{ex}	exchange-dependent relaxation rate in the rotating frame
rf	radiofrequeny
SAR	specific absorption rate (of rf energy in the tissue)
SL	spinlock
SNR	signal-to-noise ratio
SSP	steady-state pulsed
T_R	repetition time
t_{sat}	duration of saturation period
τ_c	correlation time of molecular tumbling motion
ω_a	Larmor frequency ω_a of pool a
WEX	water exchange spectroscopy
WSP	weak saturation pulse
x, y, z	rotating frame of reference
$x_{eff}, y_{eff}, z_{eff}$	effective frame of reference
Z	Z-spectrum signal ($Z = M_{sat}/M_0$)
Z_i	initial z-magnetization ($Z_i = M_i/M_0$)
Z^{ss}	steady-state Z-spectrum signal

1. Introduction

The analysis of nuclear magnetic resonance (NMR) spectra yields information on spin density, spin–spin couplings, molecular tumbling and properties related to the chemical environment of the nuclei. When applied to living tissue (*in vivo* NMR spectroscopy, MRS) one obtains noninvasively biochemical data on small and mobile metabolites (concentrations, metabolic turnover, disposition kinetics) and physiological parameters (intra-cellular pH, energy state, oxygen supply). Since the abundance in tissue of metabolites and nuclear spins other than ^{1}H is much smaller than that of water protons, molecular and non-proton MR imaging (MRI) is strongly limited *in vivo* in terms of signal-to-noise ratio, spatial resolution and scanning time.

A diluted spin system (solute pool) in aqueous solution undergoes microscopic processes which can be utilized to counteract these limitations. In particular, the relaxation of water protons (water pool) can be affected by the spin population of the dilute pool due to inter- and intra-molecular magnetization transfer (MT) processes mediated by scalar or dipolar spin–spin couplings or chemical exchange (Englander *et al* 1972, Grunwald *et al* 1962, Ward *et al* 2000). The chemical exchange between solute and water pool is employed in chemical exchange saturation transfer (CEST) experiments to indirectly detect solute pools by observing changes in the water pool (Forsen and Hoffman 1963, Ward *et al* 2000, Wolff and Balaban 1990).

During radiofrequency (rf) irradiation, transferred saturation is accumulated in the water pool resulting in a detectable alteration of the water proton signal. This signal amplification, which is in the order of the exchange rate of the process, makes possible indirect imaging—via the signal of the water pool—of metabolites of low concentration and thus overcomes a major limitation of *in vivo* MRS, at least for metabolites with exchanging protons. CEST-MRI may become a versatile technique for *in vivo* molecular imaging without radioactive tracers or exogenous contrast agents. The value of this approach is augmented by the dependence of the exchange rates on physical and physiological parameters that characterize the microenvironment such as restriction in motion, temperature, pH and metabolite concentration.

These complex relations underlie the diverse CEST effects observed *in vivo*, where CEST imaging revealed MRI contrast in studies of human brain tumors (Jones *et al* 2012, 2006, Zhou *et al* 2011), mamma carcinoma (Dula *et al* 2012, Schmitt *et al* 2011b), prostate carcinoma (Jia *et al* 2011), stroke (Sun *et al* 2007b, 2008, 2011), Alzheimer's disease (Haris *et al* 2012b, 2013) and of cartilage integrity (Haneder *et al* 2012, Krusche-Mandl *et al* 2012, Ling *et al* 2008, Schmitt *et al* 2011c, Singh *et al* 2011).

However, similar to the complex superposition of unresolved peaks, multiplets and broad macromolecular resonances that compromises *in vivo* NMR spectra, *in vivo* CEST effects are in competition with macromolecular MT (Henkelman *et al* 2001), direct water saturation (spillover effect) (Mulkern and Williams 1993, Sun and Sorensen 2008, Zaiss *et al* 2011), and concomitant saturation by other exchanging or dipolar-coupled pools (nuclear Overhauser effect, NOE) (Jin *et al* 2012b, Ling *et al* 2008, Liu *et al* 2013c). Moreover these interfering effects strongly depend on the static magnetic field strength (B_0), the rf irradiation amplitude (B_1) and other experimental parameters.

This interplay renders CEST a complex technique; hence the design of CEST experiments and the interpretation of data is an important issue. Several excellent reviews about CEST focus on data evaluation, technical issues, challenges in imaging and clinical applications (Liu *et al* 2013b, Terreno *et al* 2010, van Zijl and Yadav 2011, Vinogradov *et al* 2013, Zhang *et al* 2003, Zhou and Zijl 2006). The purpose of our review is the theoretical analysis of the physics underlying the competing saturation transfer phenomena in NMR during off-resonant irradiation into exchanging spin systems. Following recent theoretical and experimental

progress which demonstrated that saturation transfer can be described as exchange-dependent relaxation in the rotating frame, we discuss the various effects in the scope of this theory which is also valid for off-resonant spinlock (SL) (Jin *et al* 2012a, Zaiss and Bachert 2012a).

The prepared signal ($\sim M_{sat}$) is the z-component of the magnetization of the water protons. Normalized by the signal ($\sim M_0$) of the thermal-equilibrium magnetization it yields the so-called 'Z-value' $Z = M_{sat}/M_0$ (Woessner *et al* 2005). The 'Z-spectrum' (Grad and Bryant 1990) is the plot of Z-values as a function of rf irradiation frequency. To avoid confusion of the terms CEST, MT, NOE or direct saturation we suggest to designate techniques that rely on signals obtained by off-resonant irradiation by the term MR Z-spectroscopy (MRZS).

We begin with an overview on the basic phenomena and reported effects of certain exchanging sites (section 2), review theoretical treatments of continuous-wave (cw) Z-spectroscopy (section 3), and discuss the dependence of saturation transfer on B_1, the interference of effects, and technical issues (section 4). Finally, quantification approaches are discussed (section 5) and methods and proposed pulse sequences in this field are reviewed (section 6).

2. Phenomena and underlying mechanisms in Z-spectroscopy

Saturation and Z-spectrum. To utilize chemical exchange, selective labeling of the spin ensemble is needed. This can be achieved by saturation with resonant rf irradiation. For spin-1/2 systems, saturation means driving the system to equal population of spin up $|\uparrow\rangle$ and spin down $|\downarrow\rangle$ states. The macroscopic magnetization of a completely saturated spin system is zero.

In the case of chemical exchange where protons move, e.g., from sites at macromolecules or small metabolites (pool b) to water molecules (pool a) and vice versa, saturation of metabolite protons is transferred to the water pool which thereby becomes partially saturated. Hence, the spin polarization of pool a is diminished.

An alternative point of view is to understand saturation transfer as an rf-induced relaxation pathway. This relaxation takes place in the rotating frame of reference (with coordinates x, y, z in the following) and is altered by exchange. The corresponding longitudinal and transversal relaxation times are called $T_{1\rho}$ and $T_{2\rho}$. Since this effect depends on the rf irradiation frequency, one observes selectively altered $T_{1\rho}$ relaxation. The theory that describes the dynamics of the coupled magnetization vectors in spin-exchange experiments is based on the Bloch–McConnell (BM) equations (McConnell 1958).

Before we regard the BM equations and their solutions, we discuss the basic saturation transfer MR sequence and effects apparent in *in vivo* Z-spectra. An overview of reported CEST effects and underlying parameters known at present is given in table 1.

2.1. The basic saturation transfer experiment

The basic experiment for measuring saturation transfer effects consists of a presaturation with duration t_{sat} and irradiation field with amplitude $B_1 = \omega_1/\gamma$ tuned to a frequency with offset $\Delta\omega$ from the water proton resonance. This sequence is followed by excitation, spatial encoding and image data acquisition (figure 1). Saturation and readout can be sequential or interleaved.

The straightforward saturation scheme is a long rectangular pulse ($t_{sat} \gg T_1$) which is called cw irradiation. The off-resonant SL preparation consists of a 90°-phase-shifted pulse tilting the magnetization towards the z_{eff}-axis of the effective frame (with coordinates x_{eff}, y_{eff}, z_{eff}), a rectangular saturation pulse which creates an effective field which is now collinear with the magnetization, and a 90°-phase-shifted tilting pulse which flips the magnetization vector
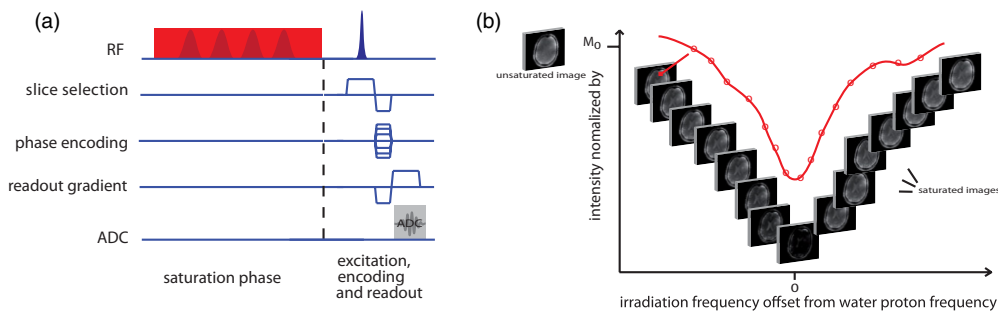
Figure 1. A saturation transfer sequence. (a) After saturation at a specific frequency the prepared magnetization is excited, spatially encoded and one or more k-space lines are acquired. This is repeated until the full k-space is sampled. The interleaving of imaging and saturation can be optimized for different applications. (b) To acquire a full Z-spectrum, the sequence of (a) is repeated for each offset frequency, leading to an image for each offset—or equivalently a Z-spectrum for each pixel. The Z-spectrum is further evaluated after normalization with an unsaturated image.
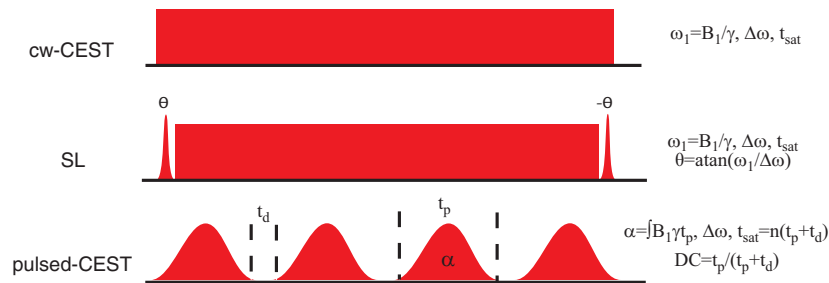

Figure 2. Saturation techniques. cw saturation consists of a rectangular pulse of width t_{sat}, frequency offset $\Delta\omega$, and rf amplitude B_1. Nearly the same contrast yields SL saturation which tilts the magnetization vector into the effective frame before saturation and back after saturation. Pulsed saturation is required in clinical MR systems due to recommended SAR limits. Pulse shape, flip angle and duty cycle provide further useful experimental parameters. The cw power equivalent was introduced regarding the pulsed case (equation (72)).

back to the z-axis in the rotating frame (x, y, z) (figure 5). Off-resonant SL and cw-CEST lead to almost the same saturation transfer contrast. In clinical MRI systems saturation is performed by trains of shaped rf pulses (figure 2), because pulse width is restricted to keep SAR below the recommended limits. A detailed overview on different presaturation schemes and saturation transfer sequences is in section 6 and in the review articles (Liu *et al* 2013b, Vinogradov *et al* 2013).

2.2. Observed effects in the in vivo Z-spectrum

Shifted frequency axis and direct water saturation.   Figure 3 shows an *in vivo* Z-spectrum obtained from rat brain tissue (Jin *et al* 2012a). The most obvious effect is the collapse of signal at 0 ppm ('water peak') caused by *direct water saturation* (Mulkern and Williams 1993, Smith *et al* 2009) of the spin system of water protons (^1H). Note that the frequency axis of Z-spectra is shifted by 4.7 ppm relative to the scale employed in conventional ^{1}H NMR spectroscopy. The direct saturation effect is mainly determined by the amplitude B_1 of the saturating rf field and T_1 and T_2 relaxation. It vanishes far off-resonance and is well described by the Bloch equations (Bloch 1946).
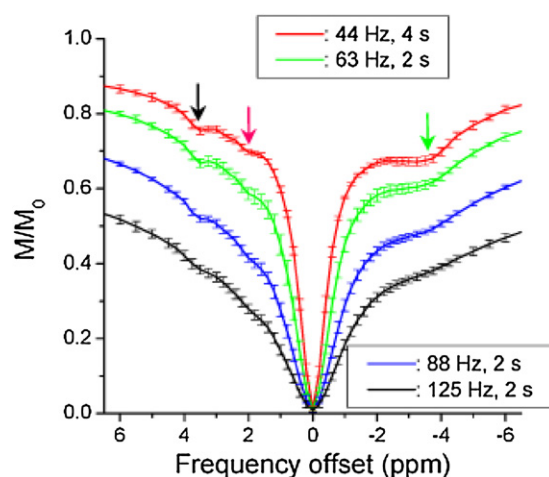
Figure 3. *In vivo* Z-spectrum, i.e. the normalized magnetization of water protons as a function of offset $\Delta\omega$ of the saturation frequency, of rat cortex obtained by off-resonant SL with 2D-spin-echo echo-planar imaging (2D-SE-EPI) at $B_0 = 9.4$ T. Direct water saturation governs the spectrum around 0 ppm (water proton resonance). The broad macromolecular MT determines the baseline. The amine and amide CEST effects are resolved at 2 ppm (red arrow) and 3.5 ppm (black arrow), respectively. Around -3 ppm contributions of aliphatic NOE are observed (green arrow). The apparent effects depend on both the saturation amplitude ($\omega_1 = \gamma B_1$ given in Hz) and duration (irradiation period in s). Major issues are B_1-dependent labeling efficiency and the selectivity of the CEST effects, the dilution of CEST effects by direct water saturation (spillover effect) and MT. Reproduced with kind permission from Jin and Kim (2012). Copyright © 2012 Elsevier.

Protons bound to different molecules show different resonance frequencies. This effect is called chemical shift, as it is caused by varying shielding of the external field B_0 by the electron cloud depending on the chemical structure. Conventionally, originating from cw NMR spectroscopy, the frequency axis is directed from upfield to downfield (from positive to negative ppm values) with respect to the resonance of a reference compound. Protons with upfield resonances experience a larger shielding, i.e. a lower local field, compared to the protons in the water molecule (resonating at 0 ppm). Accordingly, their Larmor frequencies are lower as expressed by negative ppm values. Resonances downfield from water have positive ppm values.

Semi-solid macromolecular magnetization transfer. The *semi-solid macromolecular MT* is a non-selective effect scattered across the Z-spectrum with resonance linewidths of several kHz. It results from the saturation of protons bound to the surface of macromolecules and protons in water molecules bound to the 'macromolecular matrix' (figure 4(b)), which comprises, e.g., surfaces of proteins, cell membranes and structure elements like collagen fibers in cartilage, bone and skin. The strongly broadened resonances correspond to T_2 times in the order of μs. Hence a magnetization transfer contrast (MTC) can be prepared even at large frequency offsets in the order of kHz which eventually yields a distinct tissue contrast in MRI (Henkelman *et al* 2001). Macromolecular MT is mainly governed by the proton transfer rate from the macromolecular pool to the water pool of about 40 s^{-1} (Stanisz *et al* 2005) and the concentration of the pool of protons with restricted mobility relative to that of the free pool (up to 20% in cartilage (Stanisz *et al* 2005)). MT can be modeled by the BM equations where the transverse components are neglected due to rapid T_2 relaxation of the MT pool ($R_{2b} \sim 10^5$ s^{-1}) (Henkelman *et al* 1993).

Table 1. Selection of reported *in vitro* and *in vivo* CEST effects with corresponding frequency shifts δ_b of pool b relative to pool a, sensor concentrations (pool b) and estimates of exchange rates (k_b in s^{-1}). Together with the strengths of reported effects, the corresponding experimental values of B_0, B_1 and saturation time t_{sat} are given. The optimal values were taken in cases where different B_1 and t_{sat} values were reported. Exchange rates refer either to *in vivo* conditions, otherwise conditions are given explicitly in brackets.

	Sensor or functional group (δ_b)	Sensor concentration	Reported effect (B_0, B_1, t_{sat})	Exchange rate (s^{-1}) (pH,T)
Brain	Amides ($\approx$ 3.5 ppm)	71.9 mM ($f_b = 0.65$ ‰)[1] 27.8 mM ($f_b = 0.25$ ‰)[2]	2–3% (9.4 T, 1 μT, 4 s)[3] 1–1.5% (7 T, 0.9 μT, 4 s)[2]	28.6 [1], 280 [2], 30 [28]
	Amines (2 ppm)	Contributing proteins and small molecules >0.25 ‰[2]	9% (9.4 T, 8.2 μT, 350 ms)[4]	700–10 000 [4]
	Glutamate (3 ppm)	6 mM (WM)[5] 9.4 mM (GM)[5]	7–12% (7 T, 3.6 μT, 2 s)[5]	4500 (7.0, 21 °C)[6] 2000 [5]
	Aliphatic NOE ($\approx$ –3.5 ppm)	$f_b = 2$–3%[2]	5–5.5% (9.4 T, 0.7 μT, 4 s)[3]	20–30 [2], 17[28]
	Myo–Inositol–OH ($\approx$ 0.6 ppm)	7 mM = 0.06 ‰[7]	4–5% (7 T, 4.7 μT, 6 s)[8]	600 (7.4, 25 °C)[8]
Muscle	Creatine (1.9 ppm)	40 mM[9–11]	13% (7 T, 2.9 μT, 0.5 s)[12]	950 (7.0, 37 °C)[13]
Cartilage	GAG–NH (3.5 ppm)	<375 mM[14]	1.5% (4.7 T, 0.38 μT, 8 s)[14]	Similar to amides
	GAG–OH (1–2 ppm)	<125 mM[14]	6% (7 T, 2.2 μT, 0.5 s)[15] 1% (3 T, 0.73 μT, 2 s)[15]	1000 [16,17]
Exogenous sensors (*in vitro*)	Iopamidol[18–20] amides (4.2 ppm, 5.5 ppm)	26 mM	45% (7.05 T, 3.1 μT, 7 s)[18]	2650 (7.4, 37 °C)[18] 415 6, 37 °C)[19]
	Dihydrothymidine–2[21] amide (5 ppm)	20 mM	21% (11.7 T, 5 μT,4 s)[21]	1700 (7.4, 37 °C)[21]
	PARACEST Eu-DOTA-4AmCE (10–50 ppm)[22]	100 μM[23]	0.45–2.27%[23]	2000–10000 [23]
	LipoCEST (3 ppm)	250 nM[23]	0.34–8.51%[23]	10–250 [23]
Xe—HyperCEST (*in vitro*)	Xe@Cryptophane–A (130 ppm)[24–26]	Lowest: 10 nM[25]	16% of hp (9.4 T, 25.8 μT, 20 s)[25]	n.d.
	Xe@Cryptophane–A@M13(130 ppm)[27]	Lowest: 230 fM[27]	4.8% of hp (7.05 T, 207 μT, 20 s)[27]	n.d.

Note. Amides and amines refer to average amide and amine peaks *in vivo*; NOEs are average nuclear Overhauser effects; GAG, glycosaminoglycans; GM, gray brain matter; WM, white brain matter; hp, hyperpolarization; ‰= 10^{-3}; n.d., no data. Values from: [1] Zhou *et al* (2003), [2] Liu *et al* (2013c), [3] Jin *et al* (2012b), [4] Liepinsh and Otting (1996), [5] Cai *et al* (2012), [6] Jin *et al* (2011), [7] Kreis *et al* (1993), [8] Haris *et al* (2011), [9] Op 't Eijnde *et al* (2001), [10] Robinson *et al* (1999), [11] Steenge *et al* (1998), [12] Kogan *et al* (2013), [13] Haris *et al* (2012a), [14] Ling *et al* (2008), [15] Singh *et al* (2011), [16] Hills *et al* (1991), [17] Ling *et al* (2008), [18] Aime *et al* (2005), [19] Longo *et al* (2010), [20] Longo *et al* (2009), [21] Bar-Shir *et al* (2013), [22] Terreno *et al* (2010), [23] van Zijl and Yadav (2011), [24] Schröder *et al* (2006), [25] Schröder *et al* (2008b), [26] Schröder *et al* (2008a), [27] Stevens *et al* (2012) and [28] Xu *et al* (2013a).
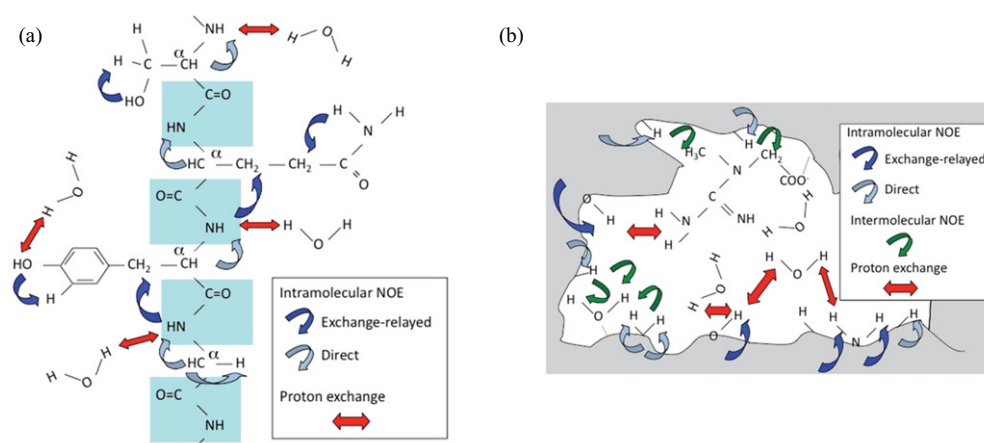
Figure 4. Illustration of possible transfer pathways. (a) Pathways in a mobile protein can proceed via chemical exchange (red) or cross relaxation (NOE) (blue). NOE can be exchange-relayed or through direct interaction. Intermolecular NOEs are small in liquids. (b) If the mobility of water molecules is restricted by the semi-solid matrix (gray), intermolecular NOEs become more important and establish together with proton exchange the pathway of macromolecular MT. Reproduced with kind permission from van Zijl and Yadav (2011). Copyright © 2011 Elsevier.

CEST effects.   In the range of positive ppm values (i.e., on the left-hand side of the water resonance) chemical-exchange effects are observed in the Z-spectrum which are caused by 'labile' protons of functional groups, for example in amide, amine and hydroxyl groups (figure 4(a), table 1). Although chemical shifts differ depending on the proton site in the molecule, an unequivocal assignment of CEST peaks in the Z-spectrum to metabolites *in vivo* is in general not possible. However, knowing contributors in specific tissue and their exchange rates, chemical shifts and relaxation parameters (table 1) allows often a correlation between apparent effects and metabolites.

Exchange processes are chemical reactions which are often base- or acid-catalyzed. Depending on the type of molecule and reaction, the exchange rates k can vary in the range of some s^{-1} (for amides (Zhou *et al* 2003)) up to several $10\,000\,s^{-1}$ (for hydroxyl protons) (Yadav *et al* 2012). The exchange rate k is a function of temperature, pH and buffer properties of the solution. The CEST effect is mainly governed by the exchange rate and the concentration of the metabolite protons relative to those of the water protons. CEST can be modeled appropriately by the BM equations (McMahon *et al* 2006, Woessner *et al* 2005, Zhou *et al* 2004).

From recent *in vivo* studies, a number of CEST phenomena of tissue metabolites has been reported (table 1). These include glycosaminoglycans (GAG) (Ling *et al* 2008, Schmitt *et al* 2012, Singh *et al* 2011), creatine (Haris *et al* 2012a, Kogan *et al* 2013), glucose (Chan *et al* 2012), glutamate (Cai *et al* 2012, Jin *et al* 2012a) and *myo*-inositol (Haris *et al* 2011, 2013). Besides those 'endogenous contrast agents' that are natural components of living tissue, exogenous CEST agents were investigated, e.g. iopamidol with two prominent amide resonances (Longo *et al* 2009) and strongly shifted paramagnetic tracers (PARACEST) such as [Eu-DOTA-4AmCE]$^{3+}$ (Zhang *et al* 2001) (for more details on PARACEST, see De Leon-Rodriguez *et al* (2009), Terreno *et al* (2010), Woods *et al* (2006) and Zhang *et al* (2003)).

Another interesting group of exogenous CEST tracers are the compartmental agents employed in LipoCEST and HyperCEST. In the former (Terreno *et al* 2007, 2008, Zhao *et al* 2008) a large number of water molecules transfers in and out of a liposome. The resonance of water protons within the compartment is shifted by a paramagnetic compound. In HyperCEST

(Meldrum *et al* 2010, Schröder *et al* 2006, Sloniec *et al* 2013, Spence *et al* 2001), a Xe atom jumps in and out an artificial cryptophane—a cage, where the cage structure induces a large chemical shift. Both experiments yield a strong signal enhancement: LipoCEST due to the number of water molecules that can contribute within the liposome, and HyperCEST due to the feature of hyperpolarization that can be generated in a ^{129}Xe ensemble by spin exchange optical pumping. Recently, an advanced HyperCEST method established the current lower detection limit of NMR at a sensor concentration of 230 fM (Stevens *et al* 2012).

Nuclear Overhauser effects.   Besides the physical transfer of protons through space, NOEs mediated by dipolar interactions between close spins provide further saturation pathways as dominant exchange-relayed NOEs and inter- and intra-molecular NOEs (van Zijl *et al* 2003). These dipolar interactions are used in dynamic nuclear polarization experiments which were first performed on heteronuclear systems of ^{19}F–^{1}H (Solomon 1955) to enhance the signal of the rare spin system (^{19}F). In the *in vivo* Z-spectrum homonuclear (^{1}H–^{1}H) NOEs are observed between water and aliphatic protons resonating in the spectral range from -2 to -5 ppm, i.e., on the right-hand side of the water peak, but also for aromatic peaks (in the range 1–4 ppm) (Jin and Kim 2013a). By the introduction of the cross-relaxation rate σ, the Bloch equations could be extended by this transfer process leading to the Bloch–Solomon (BS) equations (Solomon 1955). The cross-relaxation rate σ depends on the molecular configuration (r_{IS}) and mobility (τ_c). Presently, the influence of pH and temperature on exchange-relayed NOEs is discussed (Jin *et al* 2012b, Jones *et al* 2013) as well as the influence of the protein folding state (Zaiss *et al* 2013b). Under the assumption of an equilibrium condition $\sigma_a M_a = \sigma_b M_b$ for pools a and b the Solomon equations display the same mathematical structure as the BM equations.

Dependence of CEST effects and NOE on B_1 and saturation time.   All these effects and their resolution in the Z-spectrum strongly depend on the parameters of rf irradiation (figure 2). This important issue will be addressed in section 4.1 of this review. To assess the extent of saturation the labeling efficiency is a useful parameter which is determined by the amplitude B_1 of the rf field, the chemical-shift difference of exchanging protons at different sites and the exchange rate. Typical B_1 values for effective saturation in clinical MRI systems are in the order of μT. Direct saturation and MT effects increase with stronger saturation, while pronounced gains of CEST effects and NOE only occur at saturation amplitudes smaller than the exchange rate. Therefore, for a specific CEST/NOE effect of interest in a specific tissue, B_1 has to be optimized. Table 1 illustrates the large range of optimal B_1 values that was reported for the different exchanging groups.

In the course of saturation, experiments toward steady-state—which is called here the 'transient-state'—the CEST effects build up with a time constant in the order of T_1. Thus, T_1 yields a measure for the required saturation time t_{sat} of the system under investigation: the steady-state signal is reached after long saturation periods ($t_{sat} \sim 5 \cdot T_1$). T_1—which limits the accumulation of saturation in the water pool—also determines the size of all saturation transfer effects in steady-state and is therefore an important parameter in MRZS. For exchange effects in the intermediate range there may exist an optimal saturation time with less interference by direct saturation and MT (Jin *et al* 2011, Singh *et al* 2011). In pulsed experiments, this results in an optimal number of pulses, but also in definite delay times between the pulses that are optimal for studies of molecular systems with specific exchange rates (Jones *et al* 2013, Sun *et al* 2011, Xu *et al* 2013a, Zu *et al* 2011b).

Specific absorption rate and pulsed saturation.   For safety reasons the width t_p of rf pulses in clinical MR scanners is restricted (e.g., $t_p \leqslant 100$ ms). Trains of short pulses and appropriate

interpulse delays are employed to keep the SAR value (specific absorption rate of rf energy in the tissue) below the recommended limits (Schmitt *et al* 2011a). Pulsed saturation is a challenge for the theoretical description (see section 4.8). However, this restriction, which entails lower labeling efficiency, has also positive features: pulse trains which flip the magnetization by 180° are almost as effective as cw saturation. Moreover, using varying rotation angles also spillover- and MT-insensitive methods are feasible (Friedman *et al* 2010, Zu *et al* 2011a, 2012).

3. Theory of saturation transfer and spinlock—quantitative *Z*-spectroscopy

To model and analyze the outcome of MRZS experiments the BM equation system (McConnell 1958) is employed (Forsen and Hoffman 1963, Henkelman *et al* 1993, McMahon *et al* 2006, Trott and Palmer 2002, Wolff and Balaban 1990, Zhou and Zijl 2006, Zhou *et al* 2004). The BM equations are an appropriate tool for modeling chemical exchange (Forsen and Hoffman 1963, McConnell 1958, Wolff and Balaban 1990). In a modified form—as shown below (equation (11))—they also describe conventional MT (Henkelman *et al* 1993), where the absorption line shapes are more solid-like (Henkelman *et al* 2001, Li *et al* 2008). Moreover, MT effects in dipolar-coupled spin systems (NOE) as described by the BS equations, can be treated in the framework of the BM equations (McConnell 1958, Solomon 1955, Vinogradov *et al* 2013).

3.1. The Bloch–McConnell (BM) equations

We consider a two-pool system, i.e., a system of two coupled spin populations, comprising pool a (the water pool) and pool b (the dilute solute pool), with forward (b → a) exchange rate k_b and thermal equilibrium magnetizations $M_{0,a}$ and $M_{0,b}$, respectively, in a static magnetic field $\vec{B}_0 = (0, 0, B_0)$. The ratio of these magnetizations, $M_{0,b}/M_{0,a} = f_b$, is conserved by the backward (a → b) exchange rate $k_a = f_b k_b$. Pool a is always the pool which is measured, here and in proton CEST it is the spin ensemble of water protons. In the case of HyperCEST, pool a is that of xenon in the solvent.

The temporal evolution of the magnetizations of the two pools during rf irradiation is well described by the BM equations for the case of exchange between pools a and b and by the BS equations for dipolar-coupled systems.

In the rotating frame of reference (x, y, z) defined by the frequency ω_{rf} of the oscillating field $B_1(t)$, the BM equations read

$$\frac{d}{dt}\vec{M} = A \cdot \vec{M} + \vec{C} \tag{1}$$

with the six-dimensional magnetization vector

$$\vec{M} = \begin{pmatrix} M_{xa} \\ M_{ya} \\ M_{za} \\ M_{xb} \\ M_{yb} \\ M_{zb} \end{pmatrix}. \tag{2}$$

A is a block matrix

$$A = \begin{bmatrix} L_a - K_a & +K_b \\ +K_a & L_b - K_b \end{bmatrix} \tag{3}$$
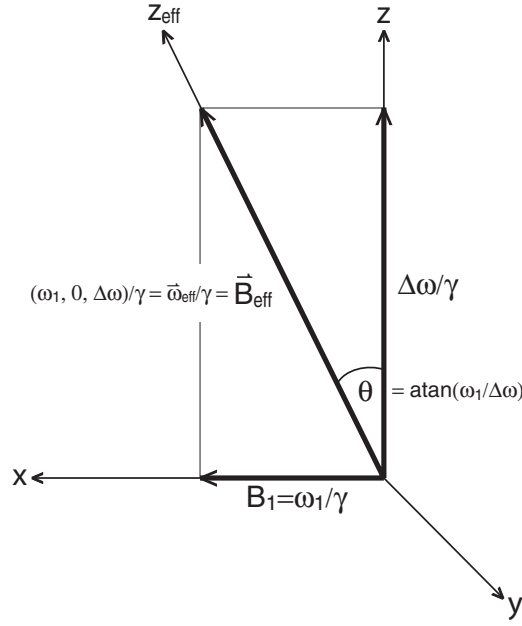
Figure 5. The effective frame defined by the effective field $\gamma \vec{B}_{\text{eff}} = \vec{\omega}_{\text{eff}} = (\omega_1, 0, \Delta\omega)$ in the rotating frame of reference (x, y, z). $\vec{B}_{\text{eff}}$ is an eigenvector of the smallest eigenvalue in modulus of the BM equation system, with absolute value $R_{1\rho}$. Thus in steady-state the magnetization vector of the system is dominated by the contribution along z_{eff}.

consisting of 3×3 submatrices $K_i = k_i \cdot \mathbf{I}$ (see equations (6), (8) and (9)), and L_i:

$$L_i = \begin{pmatrix} -R_{2i} & -\Delta\omega_i & 0 \\ +\Delta\omega_i & -R_{2i} & +\omega_1 \\ 0 & -\omega_1 & -R_{1i} \end{pmatrix} \tag{4}$$

where $i = $ a, b. Finally, the constant vector C is

$$\vec{C} = \begin{pmatrix} 0 \\ 0 \\ R_{1a}M_{0a} \\ 0 \\ 0 \\ R_{1b}M_{0b} \end{pmatrix}. \tag{5}$$

The quantity $\Delta\omega = \Delta\omega_{\text{a}} = \omega_{\text{rf}} - \omega_{\text{a}}$ is the frequency offset relative to the Larmor frequency ω_{a} of pool a (for ^{1}H: $\omega_{\text{a}}/B_0 = \gamma = 267.5$ rad μT^{-1} s^{-1}). The offset of pool b: $\Delta\omega_{\text{b}} = \omega_{\text{rf}} - \omega_{\text{b}} = \Delta\omega - \delta_{\text{b}}\omega_{\text{a}}$, is shifted by δ_{b} relative to the water proton resonance.

At field strengths of clinical MR imaging systems, longitudinal relaxation rates $R_{1,\text{a/b}} = 1/T_{1,\text{a/b}}$ are in the order of s^{-1}, while transverse relaxation rates $R_{2,\text{a/b}} = 1/T_{2,\text{a/b}}$ are in the order of 10–100 s^{-1} for *in vivo* ^{1}H systems. For macromolecules and bound water $R_{2\text{b}}$ can take values up to 10^6 s^{-1} (Stanisz *et al* 2005). On resonance, the rf irradiation field $B_1 = \vec{B}_1, 0, 0)$, with $B_1 \approx 1\ \mu$T, induces a precession of the magnetization with frequency $\omega_1 = \gamma B_1$ around the x-axis of the rotating frame in the order of several 100 rad s^{-1}. In the case of off-resonant irradiation the magnetization rotates around the effective field $\vec{B}_{\text{eff}} = (\omega_1, 0, \Delta\omega)/\gamma = \vec{\omega}_{\text{eff}}/\gamma$ which is tilted by the angle $\theta = \tan^{-1}(\omega_1/\Delta\omega)$ off the z-axis (figure 5). The population fraction f_{b} is assumed to be $<1\%$ for most CEST experiments, hence k_{a} is small compared to k_{b}. In

contrast, for MT f_b can be as large as 19% for cartilage, but is in the range of several percent for most tissues (Stanisz *et al* 2005).

The BM/BS equations pick out one relaxation pathway explicitly. We therefore separate this process and define the relaxation rates excluding this specific pathway by $R' = 1/T'_1$ and $R'_2 = 1/T'_2$ (Neuhaus and Williamson 1989).

In the context of the BM equations the used relaxation rates already exclude exchange. Therefore, $R_{1a} = R'_{1a}$ and $R_{2a} = R'_{2a}$ and the same for pool b. The matrix $K_a = f_b K_b$ reads

$$K_a = f_b K_b = f_b \begin{pmatrix} k_b & 0 & 0 \\ 0 & k_b & 0 \\ 0 & 0 & k_b \end{pmatrix}. \tag{6}$$

The proton fraction f_b is

$$f_b = \frac{M_{0b}}{M_{0a}} = \frac{n_b \cdot [b]}{n_a \cdot [a]} \tag{7}$$

where [a] and [b] are the concentrations of pool a and b, respectively, and n_a and n_b are the numbers of protons per molecule for the respective proton pools.

Dipolar cross-relaxation.   The transfer process for dipolar-coupled spin systems is quantified by the cross-relaxation rate σ, which is the difference of the probabilities W for double- (W_{2IS}) and zero-quantum (W_{0IS}) transitions in an ensemble of dipolar-coupled pairs of spins I and S: $\sigma = W_{2IS} - W_{0IS}$; $\rho = W_{0IS} + 2W_{1IS} + W_{2IS}$. To adopt the notation of the BM equations we use here a and b instead of I and S. The transition probabilities W are functions of interaction distances r_{ab} and correlation times τ_c of molecular motion (Neuhaus and Williamson 1989). The dynamics of the coupled system is described by the BS equations (Solomon 1955). Regarding the BS equations and cross-relaxation in the notation of the BM equations we obtain the rates $R_{1a} = \rho_{ab} + \sigma_{ab} + R'_{1a}$ and $R_{2a} = \nu_{ab} + \mu_{ab} + R'_{2a}$, and similarly for pool b (Neuhaus and Williamson 1989, Solomon 1955). The coupling matrices **K** for pool a and b are

$$K_b = \begin{pmatrix} -\mu_{ba} & 0 & 0 \\ 0 & -\mu_{ba} & 0 \\ 0 & 0 & -\sigma_{ba} \end{pmatrix} \tag{8}$$

$$K_a = \begin{pmatrix} -\mu_{ab} & 0 & 0 \\ 0 & -\mu_{ab} & 0 \\ 0 & 0 & -\sigma_{ab} \end{pmatrix}. \tag{9}$$

Here ρ_{ab} and ρ_{ba} are the longitudinal relaxation rates of the explicit path of dipolar coupling, as well as σ_{ab} and σ_{ba} are the z-cross-relaxation rates, ν_{ab}, ν_{ba} the transversal relaxation rates, and μ_{ab} and μ_{ba} the x–y cross-relaxation rates of pool a and b, respectively.

Bringing the BS and the BM equations in the same form by these substitutions yields the equilibrium conditions for cross-relaxation

$$\sigma_{ab} = f_b \sigma_{ba}; \; \rho_{ab} = f_b \rho_{ba}. \tag{10}$$

Setting $\mu = \sigma$, $\rho_{ab} + \sigma_{ab} = 0$ and $\nu_{ab} + \mu_{ab} = 0$, the BM and the BS equations attain identical mathematical structure. Hence, using these analogies, all discussions in the following concerning the BM equations and their solutions are directly applicable to dipolar-coupled systems. However, it must be kept in mind that σ depends on interaction distances and correlation times, whereas the exchange rate k depends on pH and temperature (Neuhaus and Williamson 1989).

For macromolecular MT one assumes that the transverse components are zero, which is justified since the T_2 times are in the order of μs. Thus, four magnetization components remain: those along the axes x, y, z for pool a and along z for the macromolecular pool (Henkelman *et al* 1993). The matrix A (equation (3)) and the vector C now read

$$A = \begin{pmatrix} -R_{2a} & -\Delta\omega_i & 0 & 0 \\ +\Delta\omega_i & -R_{2a} & +\omega_1 & 0 \\ 0 & -\omega_1 & -R_{1a} - k_a & +k_b \\ 0 & 0 & -k_b & -R_{1b} - R_{rfb} \end{pmatrix}, \tag{11}$$

$$\vec{C} = (0, 0, R_{1a}M_{0a}, R_{1b}M_{0b}). \tag{12}$$

The matrix contains a new term R_{rfb} which considers the lineshape of the macromolecular pool

$$R_{rfb}(\Delta\omega) = \omega_1^2 \pi g_b(\Delta\omega). \tag{13}$$

Different line shape functions $g(\Delta\omega)$ were employed (Henkelman *et al* 1993, 2001): Lorentzian functions for liquid pools

$$g_b(\Delta\omega)\frac{T_{2b}}{\pi[1 + (\Delta\omega \cdot T_{2b})^2]} \tag{14}$$

or Gaussian for solid-like pools. For semi-solid structures in living tissue a super-Lorentzian lineshape defined by

$$g(2\pi\Delta) = \int_0^{\pi/2} d\theta \sin\theta \sqrt{\frac{2}{\pi}} \frac{T_2}{|3\cos^2\theta - 1|} \exp\left(-2\left(\frac{2\pi\Delta T_2}{|3\cos^2\theta - 1|}\right)^2\right) \quad [8] \tag{15}$$

was shown to fit the experimental data at best including an additional dipolar reservoir (Morrison and Mark Henkelman 1995, Morrison *et al* 1995).

If modeling focuses on CEST and the range close to the water peak, also a Lorentzian line can be fitted instead of a super-Lorentzian. This means that MT can be treated like a broad CEST effect (Liu *et al* 2013c, Zaiss *et al* 2011).

For a detailed description of MT we recommend the review of Henkelman (Henkelman *et al* 2001). Analytical solutions of the modified equations (11) are explored in (Adler and Yeung 1993, Henkelman *et al* 1993, Morrison *et al* 1995, Yeung and Swanson 1992, Yeung *et al* 1994). Finally, the different two-pool models can be combined to a multi-pool system where all effects occur simultaneously (Desmond and Stanisz 2012, Li *et al* 2008, Liu *et al* 2013c, Trott and Palmer 2004).

3.2. Numerical solution of the Bloch–McConnell equations

The BM equations are first-order ordinary differential equations with an inhomogeneous term C (equation (1)). The formal solution of the BM equations is

$$\vec{M} = (\vec{M}_0 + A^{-1}\vec{C})\exp(A \cdot t_{sat}) - A^{-1}\vec{C}. \tag{16}$$

The straightforward approach to solve a higher dimensional system of ordinary differential equations is numerical integration, e.g. Runge–Kutta methods (Butcher 1987, Murase and Tanki 2011). When matrix inversion and exponentiation are performed numerically the magnetization can be calculated for constant A (Murase and Tanki 2011, Tee *et al* 2012, Woessner *et al* 2005). Then stepwise constant solutions can be utilized to construct a full time-dependent solution of the BM equations (Sun *et al* 2011, Zu *et al* 2011b). Although the numerical approach solves the problem, the insight into the intrinsic structure of Z-spectra is limited and no analytical optimization for designing experiments is possible.

3.3. Analytical solution: the eigenspace approach

The BM equations can be elegantly solved by an eigenspace approach, where **A** is transformed into a diagonal matrix (Abergel and Palmer 2004, Miloushev and Palmer 2005, Trott and Palmer 2002, 2004, Trott *et al* 2003). It was shown that for the case of off-resonant irradiation and $\omega_{\mathrm{eff}} \gg 1/T_2$ and $t_{\mathrm{sat}} \gg T_2$ the only significant contribution to the residual magnetization of the water pool arises from the magnetization along the eigenvector $\vec{v}_1$ which corresponds to the smallest eigenvalue in modulus (Jin *et al* 2012a, Zaiss and Bachert 2012a). This eigenvector is collinear with the effective field $\vec{\omega}_{\mathrm{eff}} = \vec{B}_{\mathrm{eff}}/\gamma$ (figure 5), where $\vec{\omega}_{\mathrm{eff}} = (\omega_1, 0, \Delta\omega)$, $\omega_1 = B_1/\gamma$ and $\Delta\omega = \omega_{\mathrm{a}} - \omega_{\mathrm{rf}}$ is the offset frequency of the rf field from the Larmor frequency of pool a. The effective field and the z_{eff}-axis are tilted by the angle $\theta = \tan^{-1}(\omega_1/\Delta\omega)$ off the z-axis (figure 5).

The smallest eigenvalue in modulus, λ_1, of the BM equations is identical with $-R_{1\rho}$, the negative longitudinal relaxation rate constant in the rotating frame (Trott and Palmer 2002, Zaiss and Bachert 2012a):

$$\lambda_1 = -R_{1\rho}. \tag{17}$$

Since the eigenvalue is negative, the rate is positive: $R_{1\rho} > 0$. The consequence of the fact that only λ_1 is important is that the BM equations transform to a one-dimensional system which can be solved directly. The resulting solution for the Z-spectrum, or the Z-values at each saturation offset $Z(\Delta\omega) = M_{\mathrm{sat}}(\Delta\omega)/M_0$, are described by the monoexponential decay of the z-magnetization as a function of time with the rate $R_{1\rho}$ (Zaiss and Bachert 2012a):

$$Z(\Delta\omega, t_{\mathrm{sat}}) = (P_{z\mathrm{eff}}P_z Z_i - Z^{\mathrm{ss}}(\Delta\omega)) \, \mathrm{e}^{-R_{1\rho}(\Delta\omega)t} + Z^{\mathrm{ss}}(\Delta\omega). \tag{18}$$

The initial Z-magnetization $Z_i = |M_{\mathrm{i}}|/M_0$ decays towards steady-state given by

$$Z^{\mathrm{ss}}(\Delta\omega) = P_z \frac{R_{1,\mathrm{res}}}{R_{1\rho}(\Delta\omega)}. \tag{19}$$

To differentiate from steady-state we call the state of decay, equation (18), the transient-state.

The quantities $P_{z\mathrm{eff}}$ and P_z in equations (18) and (19) are projection factors which form the link between CEST and SL experiments (see figure 6). The assumption that the components of the magnetization along all other eigenvectors of the BM system are already decayed when the signal is measured leads to the conclusion that only the projection of $\vec{M}$ onto the z_{eff}-axis is needed to model the dynamics of the monoexponential $R_{1\rho}$ decay. A CEST experiment can therefore be understood as an SL experiment with different starting magnetization given by the length of the initial magnetization vector, $Z_i = |M_{\mathrm{i}}|/M_0$, and the cosine of the angle β between this vector and the z_{eff}-axis. This suggests the definition of the projection factor $P_{z\mathrm{eff}} = \cos\beta$. Similarly, $P_z = \cos\beta'$ represents the backprojection onto the z-axis of the magnetization after saturation. As the initial and the final magnetization can be tilted from the z-direction, the values of P_z and $P_{z\mathrm{eff}}$ depend on the type of preparation of the magnetization and can adopt values in the range of -1 to 1. In particular, for an ideal SL experiment, i.e. with perfect locking of $\vec{M}$ along $\vec{\omega}_{\mathrm{eff}}$, $P_{z\mathrm{eff}} = P_z = 1$. In the case of CEST $P_{z\mathrm{eff}} = P_z = \cos\theta$. For inverted SL (iSL (Jin and Kim 2012)) the projection factors are $P_{z\mathrm{eff}} = -1$, $P_z = 1$, while for pCEST (Vinogradov *et al* 2012) $P_{z\mathrm{eff}} = -\cos\theta$ and $P_z = \cos\theta$ are appropriate.

The steady-state term Z^{ss} (equation (19)) depends on P_z, but not on $P_{z\mathrm{eff}}$. This is caused by the fact that the steady-state does not depend on the specific initial condition. The term $R_{1,\mathrm{res}}$ is the result of the transformation of the constant vector $\vec{C}$ (equation (5)) into the effective frame. $R_{1,\mathrm{res}}$ is given by the projection of $\vec{C}$ on the first eigenvector $\vec{v}_1$, yielding $R_{1,\mathrm{res}} = \vec{v}_1 \cdot \vec{C}/M_0 \approx \cos\theta R_{1\mathrm{a}}$. In contrast to P_z and $P_{z\mathrm{eff}}$, $R_{1,\mathrm{res}}$ is independent of the type of experiment. $R_{1,\mathrm{res}}$ determines the upper limit of Z^{ss} and decreases with decreasing offset $\Delta\omega$
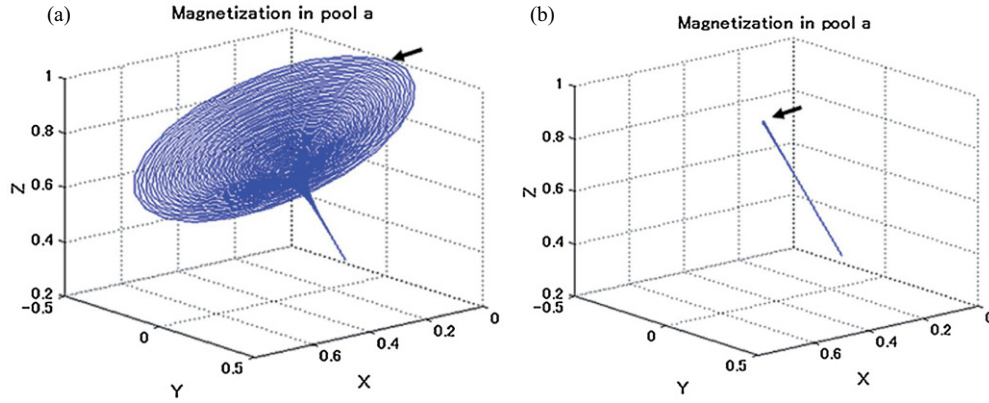
Figure 6. Trajectories of the magnetization vector of pool a under cw CEST (a) and SL preparation (b). From the starting point (arrow) the magnetization precesses around $\vec{\omega}_{\text{eff}}$. The SL pulses strongly suppress precessing components which is the nature of locking. The components of the magnetization which are not collinear with $\vec{\omega}_{\text{eff}}$ decay rapidly (time constant: $T_{2\rho}$) and effectively reduce the magnetization by the projection factor $P_{z\text{eff}}$. The components which are collinear with $\vec{\omega}_{\text{eff}}$ decay with rate $R_{1\rho}$. Parameters employed for the plots: $f_{\text{b}} = 0.03$, $T_{1a} = 1.5$ s, $T_{2a} = 0.06$ s, $T_{1b} = 0.77$ s, $T_{2b} = 0.033$ s, $\Delta\omega = 2000$ Hz and $\omega_1 = 1000$ Hz. Reproduced with kind permission from Murase (2012). Copyright © 2012 IOP Publishing.

and increasing ω_1. On-resonance ($\theta = 90°$) the residual R_1 relaxation rate vanishes ($R_{1,\text{res}} = 0$) and hence $Z^{\text{ss}} = 0$.

In the case of on-resonant SL, but also off-resonant HyperCEST, the steady-state term Z^{ss} can be assumed to be equal to 0. Therefore, equation (18) simplifies to (Zaiss *et al* 2012)

$$Z(t_{\text{sat}}) = Z_i P_z P_{z\text{eff}} \, \text{e}^{-R_{1\rho} \cdot t_{\text{sat}}}. \tag{20}$$

3.4. $R_{1\rho}$—the longitudinal relaxation rate in the rotating frame

The smallest eigenvalue in modulus for the saturation phase, $\lambda_1 = -R_{1\rho}$ (equation (17)), appears in the denominator of the expression for Z^{ss} (equation (19)). For a two-pool system, where one pool is water, $R_{1\rho}$ is the sum of R_{eff}, the water proton relaxation rate in the rotating frame and R_{ex}, the exchange-dependent relaxation rate in the rotating frame (Zaiss and Bachert 2012a):

$$R_{1\rho} = R_{\text{eff}} + R_{\text{ex}}. \tag{21}$$

R_{eff}, which equals $R_{1\rho}$ of water, can be approximated by (Trott and Palmer 2002, 2004)

$$R_{\text{eff}} = R_{1a} \cos^2\theta + R_{2a} \sin^2\theta = R_{1a} + (R_{2a} - R_{1a}) \frac{\omega_1^2}{\omega_1^2 + \Delta\omega^2}. \tag{22}$$

This effective rate follows a Lorentzian lineshape in $\Delta\omega$ with values between the baseline R_{1a} and the maximum R_{2a} and width (FWHM) $\Gamma_{\text{eff}} = 2\omega_1$ (figure 7).

3.4. R_{ex}—the exchange-dependent relaxation rate in the rotating frame.

For the determination of R_{ex} several derivations have been reported (Abergel and Palmer 2005, Trott and Palmer 2002, 2004, Trott *et al* 2003). The eigenvalue given by Miloushev and Palmer is valid even for symmetric populations (Miloushev and Palmer 2005). However, it turned out that in the case of CEST of metabolite systems asymmetric populations ($f_{\text{b}} \ll 1$) can be assumed
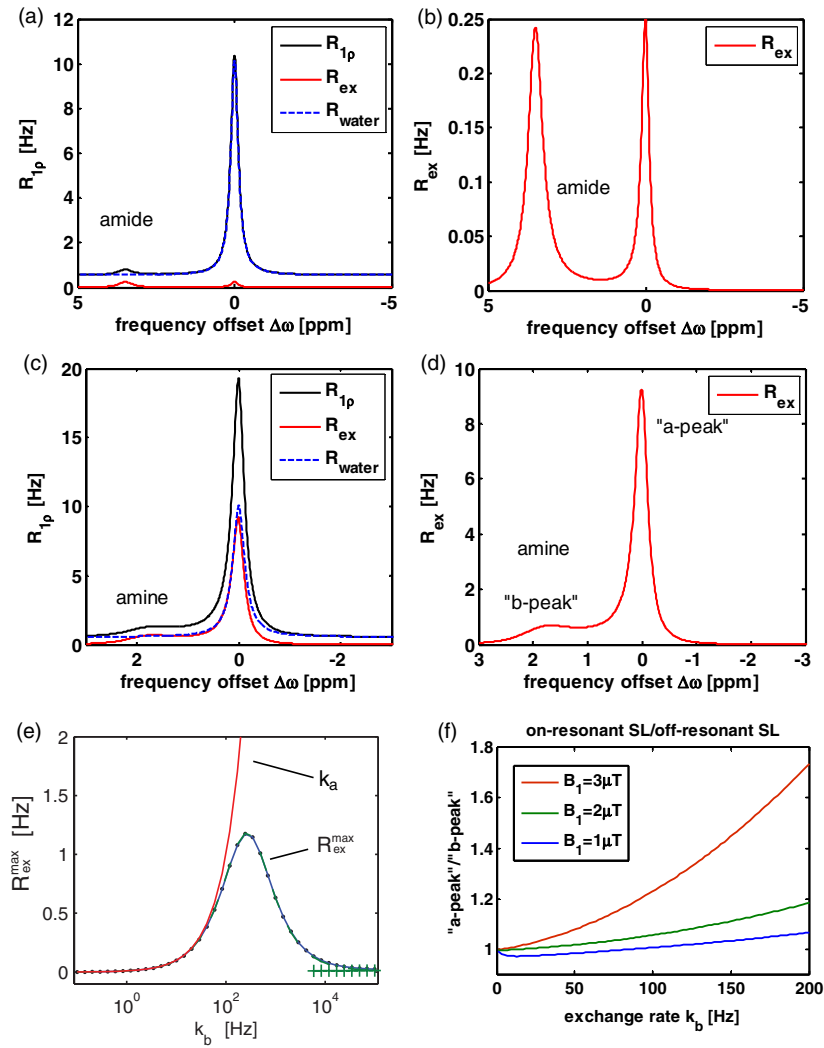
Figure 7. Spectra of the longitudinal relaxation rate in the rotating frame $R_{1\rho}(\Delta\omega)$ (black, calculated using equation (21)) for the exemplary amide (a) and amine pool (c) systems in gray brain matter at $B_0 = 7$ T and $B_1 = 1$ μT. (b), (d) Spectra of the exchange-dependent relaxation rate $R_{ex}(\Delta\omega)$. $R_{1\rho}(\Delta\omega)$ is a sum of the symmetric direct water relaxation rate $R_{eff}(\Delta\omega)$ (blue, calculated by equation (22)) and $R_{ex}(\Delta\omega)$ (red, calculated by equation (23)). The lineshape of $R_{eff}(\Delta\omega)$ is Lorentzian with baseline R_{1a}, maximum R_{2a} and FWHM $2\omega_1$. $R_{ex}(\Delta\omega)$ displays two peaks (b) and (d): they are identified in equation (23) as on-resonant on the CEST pool ('b-peak'), which is responsible for CEST effects, and on-resonant on the water pool at $\Delta\omega = 0$ ('a-peak'), which is responsible for exchange weighting in on-resonant SL experiments. For high exchange rates the a-peak becomes more prominent relative to R_{eff}, but also relative to the b-peak of R_{ex}. This is illustrated in (f) by the calculated ratio of 'a-peak' and 'b-peak' intensities. (e) R_{ex}^{max} (different approximations in blue and green, BM simulation as dots) as a function of k_b together with the full-saturation limit where $R_{ex}^{max} = k_a$ (red line). R_{ex} of equation (23) describes the observation that CEST effects first increase with the exchange rate, but decrease again when labeling (equation (38)) becomes inefficient. (e) Reproduced with kind permission from Zaiss and Bachert (2012a). Copyright © 2012 John Wiley & Sons Ltd.. Simulation parameters used, partially from Stanisz *et al* (2005)**:** water: $T_{1a} = 1.8$ s and $T_{2a} = 99$ ms; amide example system: $f_b = 0.01$, $k_b = 100$ s^{-1}, $R_{2b} = 30$ s^{-1}, $\delta\omega_b = 3.5$ ppm; amine example system: $k_b = 1000$ s^{-1}, $R_{2b} = 30$ s^{-1}, $\delta\omega_b = 1.9$ ppm, $B_0 = 7$ T.

and R_{2b} should be taken into account (Zaiss and Bachert 2012a, Zaiss *et al* 2012). Within the limit of asymmetric populations, k_a is negligible against k_b. Furthermore, the influence of R_{1b}, which is in the order of $1\ \text{s}^{-1}$, is negligible against k_b for exchanging systems with $k_b > 10\ \text{s}^{-1}$. Then, the complete formula for R_{ex} includes three terms (Zaiss and Bachert 2012a):

$$R_{ex}(\Delta\omega_b) = f_b k_b \underbrace{\underbrace{\frac{\delta\omega_b^2}{\omega_1^2 + \Delta\omega^2}}_{\text{a-peak}} \underbrace{\frac{\omega_1^2}{\Gamma^2/4 + \Delta\omega_b^2}}_{\text{b-peak}}}_{k_b\text{-term}} + f_b R_{2b} \underbrace{\frac{\omega_1^2}{\Gamma^2/4 + \Delta\omega_b^2}}_{R_{2b}\text{-term}} + f_b k_b \sin^2\theta \underbrace{\frac{R_{2b}(R_{2b} + k_b)}{\Gamma^2/4 + \Delta\omega_b^2}}_{\text{cross-term}}$$

(23)

where $\delta\omega_b = \omega_b - \omega_a$ and the linewidth Γ is

$$\Gamma = 2\sqrt{\frac{R_{2b} + k_b}{k_b}\omega_1^2 + (R_{2b} + k_b)^2}.$$

(24)

The first term, named 'k_b-term' in equation (23), dominates. It comprises the product of peaks centered at ω_a and ω_b, i.e. the Larmor frequencies of pools a and b, respectively. The 'a-peak' corresponds to the exchange-dependent relaxation observed in an on-resonant SL experiment, while the 'b-peak', together with the 'R_{2b}-term', corresponds to the exchange-dependent relaxation that yields an off-resonant peak in CEST. It is remarkable that the a- and b-peak terms occur as a product in equation (23) and therefore scale each other. The third term in equation (23) is a 'cross-term' which is neglected in the following to obtain simpler expressions; it is negligible only as long as $R_{2b}(R_{2b} + k_b) \ll \delta\omega_b^2$ which is fulfilled for amid- and amine-like systems.

In the large-shift limit (LS) ($\delta\omega_b \to \infty$) the 'a-peak' becomes 1 and $R_{ex}(\Delta\omega_b)$ simplifies to a Lorentzian line centered at $\delta\omega_b$

$$R_{ex,LS}(\Delta\omega_b) = \frac{R_{ex,LS}^{lab}\Gamma^2/4}{\Gamma^2/4 + \Delta\omega_b^2}.$$

(25)

The maximum value, $R_{ex,LS}^{lab} = R_{ex,LS}(\Delta\omega_b = 0)$, is the value of the label scan and is given by

$$R_{ex,LS}^{lab} = f_b(k_b + R_{2b})\frac{\omega_1^2}{\Gamma^2/4} = f_b k_b \frac{\omega_1^2}{\omega_1^2 + k_b(k_b + R_{2b})}.$$

(26)

This expression is similar to that derived for the weak-saturation-pulse approximation (Sun *et al* 2007a).

In the *full-saturation limit* ($\omega_1 \gg k_b + R_{2b}$ and LS) the ω_1-dependent term becomes 1 and R_{ex}^{lab} simplifies to

$$R_{ex,FS}^{lab} = f_b \cdot k_b.$$

(27)

This quantity corresponds to the exchange-dependent relaxation rate in the rotating frame of the ideal CEST effect. R_{ex} has a straightforward interpretation: for large chemical shifts and FS the relaxation rate R_{ex} equals the back exchange rate k_a. Find an overview of the approximations of $R_{1\rho}$ and R_{ex} in table 2.

Under the assumption that cross-relaxation and chemical exchange can be treated equally ($\sigma_{ba} = k_b$), this R_{ex} can also be used for modeling the influence of NOEs in Z-spectra. However, for a dipolar-coupled two-spin system also solutions for $R_{1\rho}$ are reported. This 'dipolar-R_{ex}' is a function of the spatial distance r of the interacting protons and the rotational correlation time τ_c that characterizes the time-scale of tumbling motion of the magnetic dipoles (see Mangia *et al* 2009 for details).

Table 2. Summary of important parameters of Z-spectroscopy in the general case, in the large-shift limit (LS) and in the full-saturation limit (FS).

Continuous-wave (cw) CEST in a two-pool system with asymmetric populations	General	LS ($\delta\omega_b \gg \omega_1$) at label scan	FS $\delta\omega_b \gg \omega_1 \gg k_b + R_{2b}$ at label scan
R_{eff}	$R_{\text{eff}} = R_{1a} + (R_{2a} - R_{1a})\frac{\omega_1^2}{\omega_1^2 + \Delta\omega^2}$	$R_{\text{eff}} = R_{1a}$	$R_{\text{eff}} = R_{1a}$
R_{ex}	$R_{\text{ex}}(\Delta\omega) = f_b k_b \frac{\delta\omega_b^2}{\omega_1^2 + \Delta\omega^2}\frac{\omega_1^2}{\Gamma^2/4 + \Delta\omega_b^2} + f_b R_{2b}\frac{\omega_1^2}{\Gamma^2/4 + \Delta\omega_b^2}$ $+ f_b k_b \sin^2\theta \frac{R_{2b}(R_{2b}+k_b)}{\Gamma^2/4 + \Delta\omega_b^2}$	$R_{\text{ex,LS}}^{\text{lab}} = f_b k_b \underbrace{\frac{\omega_1^2}{\omega_1^2 + k_b(k_b + R_{2b})}}_{\alpha}$	$R_{\text{ex,FS}}^{\text{lab}} = f_b \cdot k_b$
α	$\alpha = \frac{R_{\text{ex}}}{f_b k_b}$	$\alpha = \frac{\omega_1^2}{\omega_1^2 + k_b(k_b + R_{2b})}$	$\alpha = 1$
R_{ex} for $k_b \gg R_{2b}$	$R_{\text{ex}}(\Delta\omega) = f_b k_b \frac{\delta\omega_b^2}{\omega_1^2 + \Delta\omega^2}\frac{\omega_1^2}{\omega_1^2 + k_b^2 + \Delta\omega_b^2}$	$R_{\text{ex,LS}}^{\text{lab}} = f_b k_b \frac{\omega_1^2}{\omega_1^2 + k_b^2}$	$R_{\text{ex,FS}}^{\text{lab}} = f_b \cdot k_b$
Γ		$\Gamma = 2\sqrt{\frac{k_b + R_{2b}}{k_b}\omega_1^2 + (k_b + R_{2b})^2}$	$\Gamma = \infty$
MTR$^{\text{ss}} = 1 - Z^{\text{ss}}$	$1 - \frac{\cos^2\theta R_{1a}}{R_{\text{eff}} + R_{\text{ex}}}$	$\frac{R_{\text{ex}}}{R_{1a} + R_{\text{ex}}}$	$\frac{k_a}{k_a + R_{1a}}$
MTR$_{\text{asym}}^{\text{ss}}$	$\frac{\cos^2\theta R_{1a}}{R_{\text{eff}}} - \frac{\cos^2\theta R_{1a}}{R_{\text{eff}} + R_{\text{ex}}}$	$\frac{R_{\text{ex}}}{R_{1a} + R_{\text{ex}}}$	$\frac{k_a}{k_a + R_{1a}}$
MTR$_{\text{Rex}}$	$\frac{R_{\text{ex}}}{\cos^2\theta R_{1a}}$	$\frac{R_{\text{ex}}}{R_{1a}}$	$\frac{k_a}{R_{1a}}$
MTR$_{\text{asym}}(\Delta\omega, t)$	$\text{MTR}_{\text{asym}}^{\text{ss}}(\Delta\omega) + \left(P_{z\text{eff}}P_z Z_i - Z_{\text{ref}}^{\text{ss}}\right)e^{-R_{1\rho}(\Delta\omega_{\text{ref}})t_{\text{sat}}}$ $- \left(P_{z\text{eff}}P_z Z_i - Z_{\text{lab}}^{\text{ss}}\right)e^{-R_{1\rho}(\Delta\omega_{\text{lab}})t_{\text{sat}}}$	$\frac{R_{\text{ex}}}{R_{1a} + R_{\text{ex}}} + (Z_i - 1)e^{-R_{1a}t_{\text{sat}}}$ $- \left(Z_i - \frac{R_{1a}}{R_{1a}+R_{\text{ex}}}\right)e^{-(R_{1a}+R_{\text{ex}})t_{\text{sat}}}$	$\frac{k_a}{R_{1a}+k_a} + (Z_i - 1)e^{-R_{1a}t_{\text{sat}}}$ $- \left(Z_i - \frac{R_{1a}}{R_{1a}+k_a}\right)e^{-(R_{1a}+k_a)t_{\text{sat}}}$

From equation (23) one can derive an approximation of the ratio of $R_{ex}(\Delta\omega = 0)$ and $R_{ex}(\Delta\omega_b = 0)$. If R_{2b} is neglected against k_b, it follows that

$$\frac{R_{ex}(\Delta\omega = 0)}{R_{ex}(\Delta\omega_b = 0)} = 1 + \frac{\delta\omega_b^2}{\omega_1^2}\frac{k_b^2}{\omega_{eff}^2 + k_b^2}. \tag{28}$$

This shows that exchange weighting of the non-selective on-resonant SL is generally stronger than that of the off-resonant SL and thus the chemical-shift-selective CEST effect; this is even more the case for large shifts and higher exchange rates (figure 7(f)).

There exist two definitions of R_{ex}: Trott and Palmer defined (I) $R_{1\rho} = R_{eff} + \sin^2\theta R_{ex}$ (Trott and Palmer 2002), while we employed (II) $R_{1\rho} = R_{eff} + R_{ex}$ (Zaiss and Bachert 2012a). We consider (II) to be more appropriate for off-resonant SL since R_{ex} diverges in (I) in the case of the transition to large shifts (see the k_b-term in equation (23)). For on-resonant SL ($\sin^2\theta = 1$) both definitions are equivalent.

3.5. Other approaches to solve the BM equations

Although the eigenspace approach solves the initial problem we will yet review Cartesian and other techniques for solving the BM equations. Each solution requires different simplifications of the equation system. Some interesting solutions are regarded here together with the underlying assumptions.

Direct water saturation. Direct saturation is the solution for the Z-spectrum without exchange effects and was derived by Mulkern and Williams (1993). In steady-state it yields

$$Z^{ss} = \frac{R_{1a}(R_{2a}^2 + \Delta\omega^2)}{R_{1a}(R_{2a}^2 + \Delta\omega^2) + \omega_1^2 R_{2a}} \tag{29}$$

which is more precise than equation (19) with $R_{1\rho} = R_{eff}$. However, under the assumption $R_{2a} \ll \omega_{eff}$ it equals $Z = R_{1a}\cos^2\theta/R_{eff}$. Equation (29) can be used to fit the direct water saturation (Dula *et al* 2012, Jones *et al* 2012, Smith *et al* 2009).

Weak-saturation-pulse approximation (Zhou and Zijl 2006, Zhou *et al* 2004). The weak-saturation-pulse approximation is the assumption that the RF irradiation affects only the CEST pool and not the water pool. It corresponds to the large-shift limit (26). In this case rotation terms in pool a can be neglected and the Z-spectrum is given by Sun and Sorensen (2008) and Zaiss *et al* (2011):

$$Z^{ss} = 1 - \frac{k_a}{R_{1a} + k_a}\frac{\omega_1^2}{\omega_1^2 + pq + \frac{q}{p}\Delta\omega_b^2} \tag{30}$$

with (McVicar *et al* 2012)

$$p = R_{2b} + \frac{R_{2a}k_b}{R_{2a} + k_a}; \qquad q = R_{1b} + \frac{R_{1a}k_b}{R_{1a} + k_a}. \tag{31}$$

Strong-saturation-pulse approximation (Baguet and Roby 1997). For this approximation the entire BM system (longitudinal and transverse components) is transformed into a double-tilted system of the effective frames of each pool. The pools a and b characterized by their offset frequencies $\Delta\omega_a$ and $\Delta\omega_b$ are associated with effective frames defined by $(\omega_1, 0, \Delta\omega_a)$ and $(\omega_1, 0, \Delta\omega_b)$, respectively, tilted by either θ_a or θ_b with respect to the z-axis. In steady-state and under the assumption of a strong saturation field compared to exchange and relaxation

($\omega_{\text{eff}} \gg R_{2\text{a,b}} + k_{\text{a,b}}$, $\omega_{\text{eff}} \gg R_{1\text{a,b}} + k_{\text{a,b}}$, and $\omega_{\text{eff}} \gg k_{\text{a,b}}$) several terms can be neglected and one obtains

$$Z^{\text{ss}} = \cos\theta_{\text{a}} \cdot \frac{R_{1\text{a}} \cdot R_{Z\text{a}} \cdot \cos\theta_{\text{a}} + R_{1\text{b}} k_{\text{b}} \cos\theta_{\text{b}} \cos(\theta_{\text{b}} - \theta_{\text{a}})}{R_{Z\text{a}} R_{Z\text{b}} - k_{\text{a}} k_{\text{b}} \cos^2(\theta_{\text{b}} - \theta_{\text{a}})} \tag{32}$$

with $R_{Z\text{a}} = \cos^2\theta_{\text{a}}(R_{1\text{a}} + k_{\text{a}}) + \sin^2\theta_{\text{a}}(R_{2\text{a}} + k_{\text{a}})$ and $R_{Z\text{b}} = \cos^2\theta_{\text{b}}(R_{1\text{b}} + k_{\text{b}}) + \sin^2\theta_{\text{b}}(R_{2\text{b}} + k_{\text{b}})$, which yield a valid solution of the Z-spectrum for large B_1 amplitudes.

MT approximation (Henkelman *et al* 1993). The conventional MT effect is characterized by very broad resonances, which means that transverse components of the motionally restricted pool decay very fast. It is therefore justified to ignore the exchange effects of the transverse magnetization components of each pool. This approximation allows to solve the BM equations analytically in Cartesian coordinates giving the longitudinal magnetization components

$$Z^{\text{ss}} = \frac{R_{1\text{b}} \cdot k_{\text{a}} + R_{1\text{a}}(R_{1\text{b}} + R_{\text{rfb}} + k_{\text{b}})}{(R_{1\text{a}} + R_{\text{rfa}} + k_{\text{a}})(R_{1\text{b}} + R_{\text{rfb}} + k_{\text{b}}) - k_{\text{a}} k_{\text{b}}} \tag{33}$$

with the lineshape functions R_{rfa} and R_{rfb} of equation (13) which can be Lorentzian, Gaussian or other depending on the observed system (Henkelman *et al* 1993, Morrison and Mark Henkelman 1995).

4. From the ideal saturation transfer effect to a real Z-spectrum–labeling, selectivity, and concomitant effects

Knowing the contributors to the Z-spectrum, namely $R_{1,\text{res}}$ (residual $R_{1\text{a}}$), the projection factors P_z and $P_{z\text{eff}}$ and—most important—$R_{1\rho}$ with R_{eff} and R_{ex} we can now calculate the emerging CEST signal and Z-spectra (figure 8).

In an ideal CEST experiment water is solely the mediator and no direct effects of the water pool will contribute to the Z-spectrum. Accordingly, we assume a large chemical shift of the pool b where $\cos\theta = 1$ which leads to $R_{\text{eff}} = R_1$ via equations (21), (22) and (19) and to a decay with the rate $R_{1\rho} = R_1 + R_{\text{ex}}$ toward the steady-state magnetization in the large-shift limit:

$$Z_{\text{LS}}^{\text{ss}} = \frac{R_{1\text{a}}}{R_{1\text{a}} + R_{\text{ex,LS}}(\Delta\omega)}. \tag{34}$$

The difference in the Z-spectrum between a system with ($R_{\text{ex}} > 0$) and without ($R_{\text{ex}} = 0$) exchanging pool defines the maximum magnetization transfer ratio MTR in the large-shift limit

$$\text{MTR}_{\text{LS}} = 1 - Z_{\text{LS}}^{\text{ss}} = \frac{R_{\text{ex,LS}}(\Delta\omega)}{R_{1\text{a}} + R_{\text{ex,LS}}(\Delta\omega)}. \tag{35}$$

In the limit of FS (equation (27)) for the label scan, $R_{\text{ex,FS}}^{\text{lab}}$ and k_{a} are equal, hence (equation (35)) simplifies to the well-known relation (Zhou *et al* 2004)

$$\text{MTR}_{\text{FS}}^{\text{lab}} = \frac{k_{\text{a}}}{R_{1\text{a}} + k_{\text{a}}}. \tag{36}$$

In CEST theory this quantity is also called the ideal proton transfer ratio $\text{PTR}_{\text{ideal}}$ and is derived from the BM equations in Cartesian coordinates (Zhou and Zijl 2006, Zhou *et al* 2004). We indicate by 'FS' that the approximation is only valid in the case of full-saturation ($\delta\omega_{\text{b}} \gg \omega_1 \gg k_{\text{b}} + R_{2\text{b}}$). This expression gives us the CEST signal strength for an ideal system without direct water saturation or MT effects in the full-saturation limit (equation (27)).
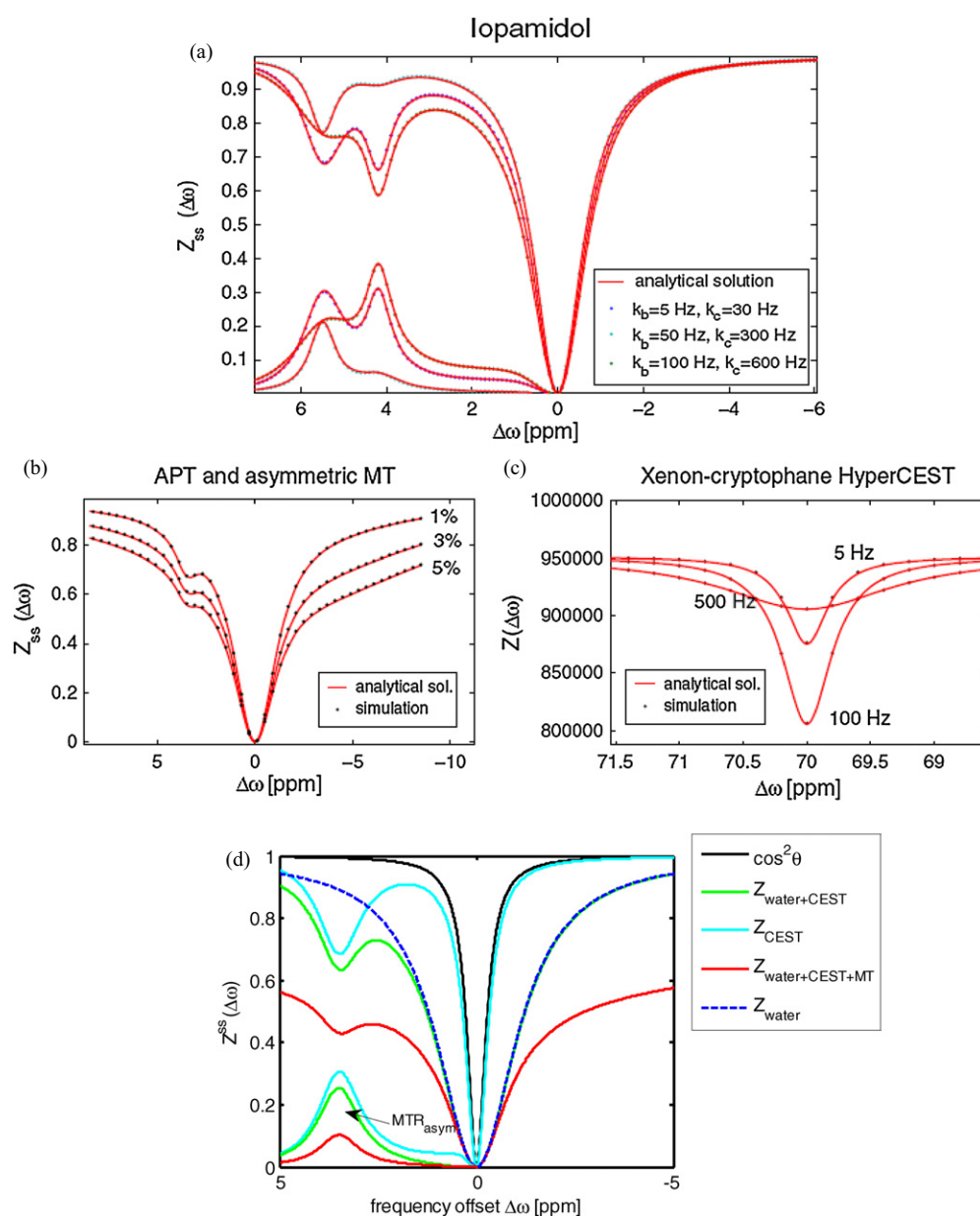
Figure 8. Simulated Z-spectra (dots) and analytic Z-spectra (lines, equation (18)) and the result of asymmetry analysis (lower left corner in (a) and (d)). The theory describes three-pool systems such as (a) iopamidol (Aime *et al* 2005), (b) APT with asymmetric MT and also the (c) Xenon-HyperCEST system (Zaiss *et al* 2012). (d) shows simulated Z-spectra of the amide proton example system in gray brain matter at $B_0 = 7$ T and $B_1 = 2 \mu$T with (red) and without MT (green). The ideal effect without MT and without direct water saturation (turquoise) is diluted by direct saturation (blue dashed) and MT. For CEST preparation the numerator is governed by the factor $\cos^2\theta$ (black). (a)–(c) Reproduced with kind permission from Zaiss and Bachert (2012a). Copyright © 2012 John Wiley & Sons Ltd.. (d) Parameters used, partially from Stanisz *et al* (2005): water: $T_{1a} = 1.8$ s and $T_{2a} = 99$ ms; MT: $T_{1mt} = T_{1a}$, $f_{mt} = 0.05$, $T_{2mt} = 9.1 \mu$s, $k_{mt} = 40$ s^{-1}, $\delta\omega_{mt} = 0$ ppm; amide example system: $f_b = 0.01$, $k_b = 100$ s^{-1}, $R_{2b} = 30$ s^{-1}, $\delta\omega_b = 3.5$ ppm; $B_0 = 7$ T.

Employing the proton fraction f_b one can estimate the signal enhancement, originally called proton transfer enhancement PTE (Zhou *et al* 2004)

$$\text{PTE} = \text{MTR}_{\text{FS}}^{\text{lab}} / f_b = \frac{k_b}{R_{1a} + k_a}. \tag{37}$$

This shows that the enhancement of transfer effects of protons of diluted solutes is almost proportional to the exchange rate k_b of the exchanging pool. Find an overview of the approximations of the MTRs in table 2.

4.1. Labeling efficiency

To explore the dependence of CEST effects on the B_1 amplitude, the labeling efficiency α is helpful (Zhou and Zijl 2006, Zhou *et al* 2004). This parameter α, which was introduced by Sun *et al* (2005a), takes values between 0 and 1 and yields a measure of the quality of the saturation in terms of the ideal CEST effect (equation (27)), where $R_{\text{ex}} = f_b k_b$. Employing α, $R_{\text{ex}}^{\text{max}}$ can now be written as

$$R_{\text{ex}}^{\text{max}}(\Delta\omega, \omega_1) = f_b k_b \cdot \alpha(\Delta\omega, \omega_1). \tag{38}$$

If taken into equation (35), lower labeling efficiency reduces the maximal effect and hence the signal enhancement according to

$$\text{MTR}_{\text{max,LS}} = \frac{k_a \cdot \alpha}{R_{1a} + k_a \cdot \alpha}. \tag{39}$$

When compared with the result of Zhou *et al* (2004) for Cartesian coordinates, the eigenspace approach (Zaiss and Bachert 2012a) shows that the labeling efficiency also appears in the denominator of MTR_{max}. For the whole CEST peak, α was first given by Sun *et al* (2007a) employing the weak-saturation-pulse approach in the Cartesian case (see equation (30)). Neglecting the cross-term in equation (23), α can be extended (Zaiss and Bachert 2012a) to

$$\alpha(\Delta\omega, \omega_1) = \frac{\delta\omega_b^2}{\omega_1^2 + \Delta\omega^2} \left(1 + \frac{R_{2b}}{k_b}\right) \frac{\omega_1^2}{\Gamma^2/4 + \Delta\omega^2} \tag{40}$$

where Γ is defined in equation (24). On-resonant on the pool b this expression simplifies to

$$\alpha = \frac{\frac{\delta\omega_b^2}{\omega_1^2 + \delta\omega_b^2} k_b + R_{2b}}{k_b + R_{2b}} \frac{\omega_1^2}{\omega_1^2 + k_b(k_b + R_{2b})}. \tag{41}$$

Hence the labeling efficiency does not only depend on the exchange rate, but also on the chemical shift $\delta\omega_b$ of pool b relative to water. As displayed in figure 9 the labeling efficiency α reaches an optimum for a specific ω_1 which is discussed in the following section. Only in the large-shift limit we obtain a monotonous dependence of α on ω_1:

$$\alpha_{\text{LS}} = \frac{\omega_1^2}{\omega_1^2 + k_b(k_b + R_{2b})}. \tag{42}$$

For ω_1 adjusted to the exchange rate via $\omega_1 = \gamma B_1 = k_b$, a labeling efficiency of about 0.5 is reached (R_{2b} small). Again for large ω_1 compared to k_b, $\alpha = 1$, which is the definition of the full-saturation limit. In this case MTR changes to equation (36) derived above. The effect in the Z-spectrum, MTR, rises when ω_1 is increased and reaches a maximum when R_{ex} and the labeling coefficient are maximal. In the full-saturation limit ($\alpha \cong 1$) MTR does not depend on ω_1, while for partial saturation ($\alpha < 1$) MTR depends strongly on ω_1. Note that for $k_b \gg \omega_1$ equation (42) can be approximated by $\alpha \approx \frac{\omega_1^2}{k_b}$, which shows that labeling is even suppressed by k_b. Altogether, we see that matching ω_1 to the exchange rate of the labile proton of interest is crucial for the experiments.
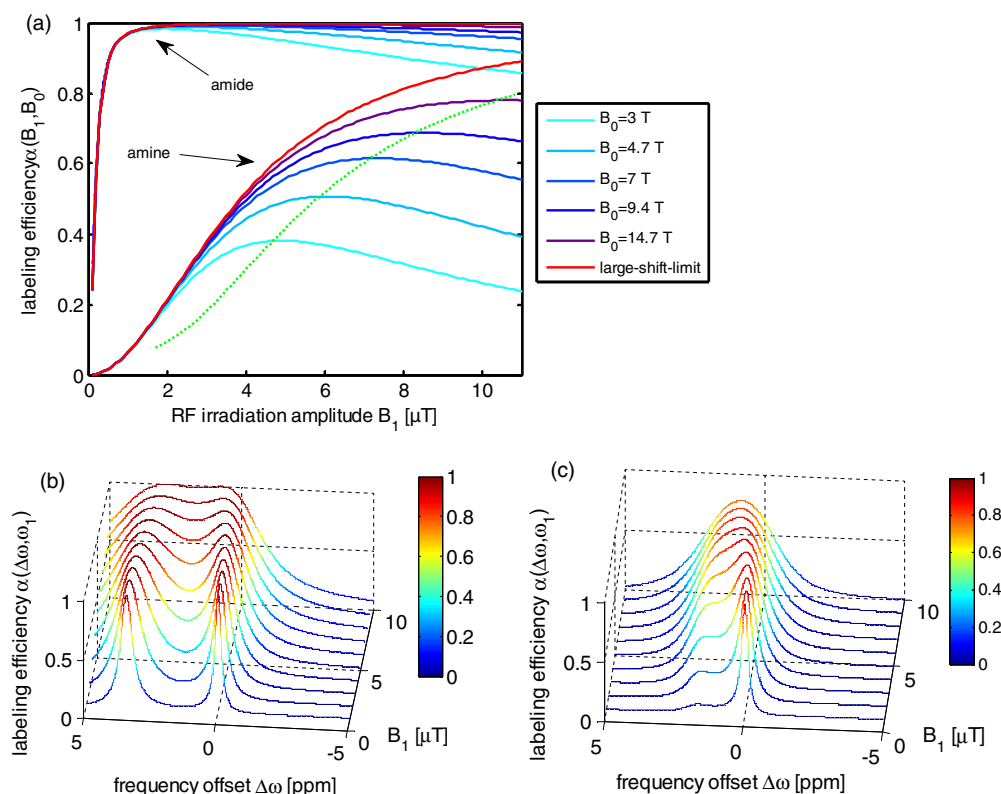
Figure 9. The labeling efficiency α for the exemplary amide and amine systems calculated by equation (41). α gives the fraction of the maximal CEST effect that can be attained. (a) α depends strongly on B_0 and B_1 and has a maximum given by equation (44) (green dashed line) at the optimal B_1 (equation (43)). While slowly exchanging amide protons are already close to full-saturation at $B_1 = 1$ μT, the labeling of faster exchanging amine protons is only about 0.05 at 1 μT. The large-shift approximation (red, equation (42)) is a monotonous function of B_1. B_1 and hence labeling can be increased by means of B_0 or the use of agents with larger chemical shifts. The decrease of labeling can be understood as the interference of the 'a-peak' and 'b-peak' in R_{ex} of equation (23) (see figure 7(f)). (b)–(c) the labeling efficiency α as a function of frequency offset $\Delta\omega$ and B_1 for amide (b) and the amine (c) example system calculated using equation (23). Labeling, but also peak width, increase with larger B_1. For too high B_1 the a-peak and b-peak of R_{ex} overlap and selectivity is lost for both systems. This again demonstrates that the rf field amplitude B_1 is a crucial parameter for MRZS determining both the strength of the effect and selectivity (exchange regimes, see section 4.3, equation (48) and figure 10). Parameters used: amide example system: $f_b = 0.01$, $k_b = 100$ s^{-1}, $R_{2b} = 30$ s^{-1}, $\delta\omega_b = 3.5$ ppm; amine example system: $k_b = 1000$ s^{-1}, $R_{2b} = 30$ s^{-1}, $\delta\omega_b = 1.9$ ppm, $B_0 = 7$ T.

4.2. Optimal labeling

To reach the maximum CEST effect the labeling efficiency has to be optimized. As reported in Jin *et al* (2012a) and Woessner *et al* (2005), optimal labeling is obtained if $k_b \approx \omega_1$. If we neglect R_{2b}, the maximum of equation (41) for MTR$_{max}$ leads to a different optimum of α for the frequency

$$(B_{1,\text{opt}} \cdot \gamma)^2 = \omega_{1,\text{opt}}^2 = \delta\omega_b k_b \qquad (43)$$

which yields the optimum B_1 amplitude for labeling an exchanging pool at a specific resonance frequency $\delta\omega_b$ (green dashed line in figure 9(a)). Then the maximum labeling efficiency is given by

$$\alpha(B_{1,\text{opt}}) = \left(\frac{\delta\omega_b}{\delta\omega_b + k_b}\right)^2. \tag{44}$$

As examples we consider two systems at $B_0 = 7$ T: for an amid-like system ($k_b = 100$ s^{-1}, $\delta\omega_b = 3.5$ ppm) optimal labeling of $\alpha = 0.99$ is attained with $B_{1,\text{opt}} = 1.51$ μT, while for an amine-like system ($k_b = 1000$ s^{-1}, $\delta\omega_b = 1.9$ ppm) $B_{1,\text{opt}} = 7.1$ μT yields $\alpha = 0.61$. In general, higher exchange rates require higher B_1 amplitudes to achieve the same labeling (Sun *et al* 2005a, Woessner *et al* 2005). Larger chemical shifts (or larger field strengths) lead to increased labeling efficiencies; hence, lower B_1 amplitudes can be applied (figure 9).

These optimal parameter values refer exclusively to labeling efficiency. If concomitant effects, such as spillover and MT, are present, $B_{1,\text{opt}}$ and labeling will decrease. This will be discussed in section 4.4. However, the optimal labeling gives us a good estimation of an upper limit for the B_1 amplitude. It also explains why the search for agents with amino groups with large chemical shifts (Bar-Shir *et al* 2013, Longo *et al* 2009, 2010) or extremely shifted agents such as PARACEST (Terreno *et al* 2010, Zhang *et al* 2003) or HyperCEST (Schröder *et al* 2006) are of considerable interest for CEST signal enhancement.

4.3. Selectivity and exchange regimes

Up to now we focused on the strength of the CEST effects. However, not only the amplitude of the peaks in the Z-spectrum, but also the selectivity changes depending on the exchange rate and B_1 of the rf field used for saturation. We assume that the large-shift limit (equation (26)) is valid where the width Γ of the Lorentzian-shaped function R_{ex} is given by equation (24). Γ can be expressed by the labeling efficiency α in the large-shift limit (42)

$$\Gamma = 2\sqrt{\frac{k_b + R_{2b}}{k_b}\omega_1^2 + (k_b + R_{2b})^2} = 2\frac{1}{\sqrt{1 - \alpha_{\text{LS}}}}(k_b + R_{2b}). \tag{45}$$

There is a minimal width $\Gamma_{\text{min}} = 2(k_b + R_{2b})$ for low saturation amplitude ω_1, i.e. small labeling efficiency α. Γ_{min} is similar to the homogeneous linewidth in the NMR spectrum $\Delta\omega_{\frac{1}{2}} = 2R_2$. On the other hand, for high saturation power, the width is asymptotically a linear function of B_1 (figure 10(a))

$$\frac{\Gamma}{\gamma} = 2\sqrt{\frac{k_b + R_{2b}}{k_b}}B_1. \tag{46}$$

Hence the peak width in the Z-spectrum and accordingly the spectral selectivity of a CEST experiment strongly depend on B_1. Balancing is needed between optimization of labeling and selectivity. For the case $k_b \approx \omega_1$ which corresponds to $\alpha \approx 0.5$ the width is insignificantly increased to $\Gamma = \sqrt{2}\Gamma_{\text{min}}$; for $\alpha \approx 0.75$ we obtain $\Gamma = 2\Gamma_{\text{min}}$ according to equation (45). Higher labeling is paid by extreme linebroadening. At maximum labeling efficiency $\alpha = 1$ the peak width has a pole (figure 10(b)).

The spectral width of effects in MRZS is also important for the offset sampling rate since the sampling distance should be in the range of Γ. Conversely, the width Γ can also be adjusted to the sampling distance via B_1.
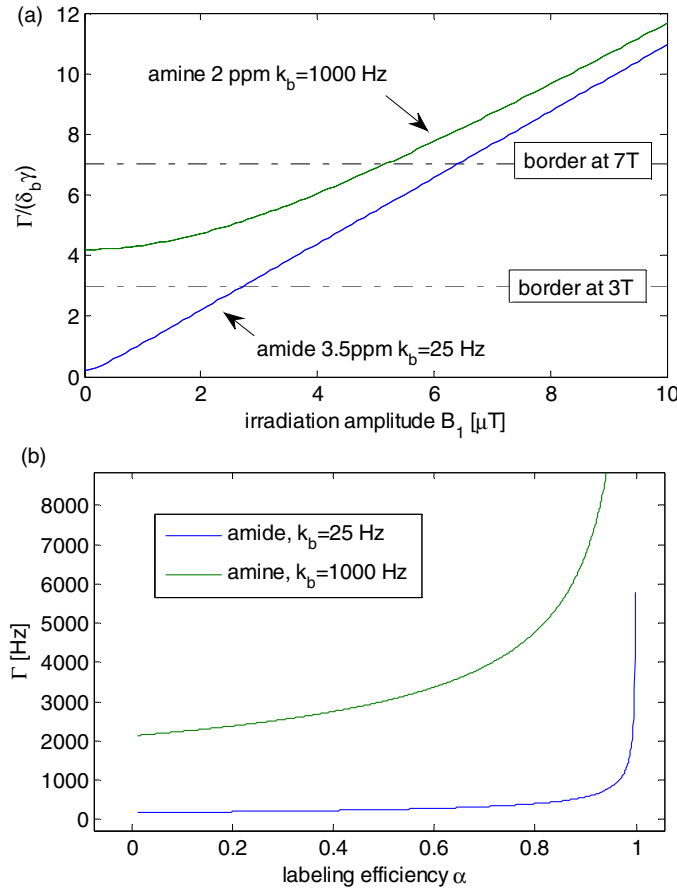
Figure 10. (a) The linewidth Γ in the Z-spectrum divided by $\delta_b\gamma$ as a function of B_1 (δ_b = chemical shift of pool b). Three selectivity regimes are discriminated: broad, intermediate and narrow. The selectivity regime changes depending on the static field strength B_0 and the applied saturation amplitude B_1. The border between narrow and intermediate in terms of $\Gamma/(\delta_b\gamma)$ is given by B_0 in T (dashed lines). If $\Gamma/(\delta_b\gamma)$ is much larger than this field, we are in the broad regime. (b) Linewidth Γ as a function of the labeling efficiency α. Γ has a pole at $\alpha = 1$, while $\Gamma(\alpha = 0.75) = 2\Gamma_{min}$. Labeling larger than 0.75 is unfavorable for selectivity. Parameters of example systems are as given in the caption of figure 7.

The peak width also allows to define a more general exchange regime. In NMR spectroscopy the spectral resolution is determined by the field strength B_0, the chemical shift and the exchange rate. The values of these parameters define three regimes:

$$k_b \begin{cases} \gg \delta\omega_b \text{ (fast)} \\ \approx \delta\omega_b \text{ (intermediate)} \\ \ll \delta\omega_b \text{ (slow)}. \end{cases} \tag{47}$$

However, in saturation transfer experiments also the amplitude B_1 of the saturating field is important for spectral selectivity. Since B_1 affects the shape of the peak we suggest a *selectivity regime in* addition to the *exchange regime*, which labels broad, intermediate and narrow linewidths in the Z-spectrum according to the values of ω_1, $\delta\omega_b$, R_{2b} and k_b:

$$\Gamma/2 = \sqrt{\frac{k_b + R_{2b}}{k_b}\omega_1^2 + (k_b + R_{2b})^2} = \frac{1}{\sqrt{1-\alpha}}(k_b + R_{2b}) \begin{cases} \gg \delta\omega_b \text{(broad)} \\ \approx \delta\omega_b \text{(intermediate)} \\ \ll \delta\omega_b \text{(narrow)}. \end{cases} \tag{48}$$

Even for a slowly exchanging amid system with $k_b \approx 100 \text{ s}^{-1}$ and $\delta\omega_b$ (3.5 ppm, 7 T) $\approx$ 6500 s^{-1} the size of $\alpha(B_1)$ still determines the *selectivity regime* of the resulting peak. Spectral selectivity requires to avoid the broad regime; hence, B_1 must be kept as low as possible, while simultaneously ensuring sufficient labeling efficiency (see (figure 10(a)).

4.4. Concomitant effects, spillover and residual T_{1a}

All saturation transfer effects are mediated by the water pool. This leads to three basic problems:

(1) All effects are scaled by the residual T_1-relaxation of water R_{1a}. In steady-state, longer T_1 leads to larger apparent CEST effects since there is more time for the labeled state to transfer into the water pool. The actual R_1 in the tilted effective frame, which we call the residual rate $R_{1,\text{res}}$, is given by $R_{1,\text{res}} = \frac{\vec{v}_1 \cdot \vec{C}}{M_0} \approx \cos\theta \cdot R_{1a}$. It is not only affected by ω_1 and $\Delta\omega$, but also by the longitudinal relaxation rates of other pools.

(2) Direct water saturation occurs—spillover effect. Without any exchanging site the water magnetization becomes smaller due to direct saturation of the water pool. Because of this saturation the CEST effects become diluted—this phenomenon is called spillover dilution. It means that less water magnetization is left for preparation by saturation transfer. Spillover dilution is larger for short T_2 and high B_1 amplitudes. In our definition, spillover only includes effects that result from water relaxation in the rotating frame governed by R_{eff}. Another direct water effect is the loss of magnetization due to the projection into the effective frame and spoiling, as modeled by the projection factors P_z and $P_{z\text{eff}}$.

(3) Concomitant magnetization transfer. In living tissue many different exchanging sites are present at the same time. The most important is concomitant semi-solid MT, but also saturation transfer of nearby exchanging pools or dipolar-coupled systems (NOE) is significant. In label scans, concomitant effects overlay the signal at offsets of interest and can reduce the specificity or induce similar dilution effects as spillover. The appropriate treatment of multi-pool systems is demonstrated in section 4.6. Problems of concomitant effects in the reference value are discussed in section 4.5.

In this section we focus on strategies to understand and solve these issues.

(1) T_1-relaxation compensation. Even without any spillover effect in the full-saturation limit the MTR is scaled by the longitudinal relaxation rate of the water pool R_{1a}:

$$\text{MTR}_{\text{FS}} = \frac{k_a}{R_{1a} + k_a}. \tag{49}$$

This induces artifacts in the MTR contrast (Wu *et al* 2012). A simple evaluation method proposed by Wu *et al* merely transforms MTR to a T_1-compensated CEST rate CESTR $= R_{1a} \cdot \text{MTR}/(1-\text{MTR})$ $R_{1a} = k_a$ which is independent of T_1.

   Also after spillover correction (equation (55)) R_{1a} determines the size of steady-state effects. Thus elimination of R_{1a}, or at least knowledge about it, is highly important for the interpretation of CEST. By the investigation of the steady-state Z-spectrum $Z \approx R_{1a}/R_{1\rho}$ it occurs that a T_{1a} compensated Z-spectrum $(Z \cdot T_{1a})$ depends on $R_{1\rho}$ only. Important to note is that transient-state methods can measure $R_{1\rho}$ directly and therefore yield an unscaled R_{ex}.

(2) Spillover correction. Spillover and concomitant effects can be removed by use of a reference scan which has no contribution of the saturation transfer effect of interest. If we leave the assumption of large shifts (equation (35)), the direct water saturation (R_{eff}, equation (22)), the residual T_1 relaxation $R_{1\text{res}} = R_{1a}\cos\theta$ and the projection factors must

be taken into account in an MTR. The generalization of the formula for the steady-state MTR defined by equation (35) by the inclusion of these effects (equation (19)) yields

$$MTR = 1 - Z_{lab}^{ss} = \frac{R_{eff} + R_{ex} - R_{1res}P_z}{R_{eff} + R_{ex}}. \tag{50}$$

We see that MTR is affected by R_{eff}, R_{1res} and P_z. By considering direct effects this MTR is no more a measure for transferred magnetization alone. The MTR is spillover-contaminated compared to the ideal value $MTR_{lab,LS}$ of equation (35); this biases quantification (see figure 13).

A zero-order correction of spillover can be achieved by using, in addition to the label Z-value Z_{lab}, some reference Z-value Z_{ref} which reflects exclusively direct saturation effects and contains no contributions from exchange processes (in section 4.5 we show how this reference value can be obtained):

$$Z_{ref}^{ss} = \frac{R_{1res}P_z}{R_{eff}}. \tag{51}$$

This reference Z-value can be obtained by a fit of direct saturation. However, often the opposite frequency offset is used and therefore this common 'zero-order-spillover correction' was called MTR_{asym} (Zhou *et al* 2004, 2003):

$$MTR_{asym} = Z_{ref}^{ss} - Z_{lab}^{ss} = \frac{R_{ex} \cdot R_{1a}P_z \cos\theta}{R_{eff}(R_{eff} + R_{ex})}. \tag{52}$$

The comparison of equation (52) with equation (50) shows that in the numerator R_{eff} and thereby the R_{2a} terms have vanished. To manage the residual R_{eff} terms in the denominator higher-order-spillover corrections can be applied. One approach is the normalization of MTR_{asym} by a reference scan as suggested by Liu *et al* (2010).

$$MTR_{refnorm} = \frac{Z_{ref}^{ss} - Z_{lab}^{ss}}{Z_{ref}^{ss}} = \frac{R_{ex}}{R_{eff} + R_{ex}}. \tag{53}$$

In contrast to MTR_{asym} (equation (52)), in the numerator the projection P_z and the residual R_{1a} relaxation term and in the denominator one R_{eff} factor have vanished. Hence, we call this a 'first-order-spillover correction'. The remaining R_{eff} in the denominator still dilutes the exchange-dependent signal (figure 11).

Recently two 'second-order-spillover corrections' were proposed to get rid of R_{eff} in the denominator of equation (52). One correction arose from an approach of probabilistic combined modeling MTR_{pcm} (Zaiss and Bachert 2012a, Zaiss *et al* 2011):

$$MTR_{pcm} = \frac{Z_{ref}^{ss} - Z_{lab}^{ss}}{Z_{ref}^{ss} - Z_{lab}^{ss} + Z_{ref}^{ss}Z_{lab}^{ss}} = \frac{R_{ex}}{R_{1a}P_z \cos\theta + R_{ex}}. \tag{54}$$

Equation (54) contains no R_{eff} terms anymore, but still P_z and residual R_{1a}. It is very close to the ideal MTR_{max} of equation (35) (figure 11). The same order of correction, but an even simpler calculation yields MTR_{Rex} (Zaiss and Bachert 2012a)

$$MTR_{Rex} = \frac{1}{Z_{lab}^{ss}} - \frac{1}{Z_{ref}^{ss}} = \frac{R_{ex}}{R_{1a}P_z \cos\theta}. \tag{55}$$

MTR_{Rex} is approximately R_{ex} in units of R_{1a}. Thus, this MTR has again to be compensated for T_1 as described in the previous section. However, if $\theta > 10°$, changes in P_z and $\cos\theta$ become important, but can easily be dealt with by employing B_0 and B_1 field maps. Equations (54) and (55) are related by the equivalence $MTR_{pcm} = MTR_{Rex}/(1 + MTR_{Rex})$. An experimental comparison of the above spillover corrections is given in Zaiss *et al* (2013a). The spillover correction reconstructs the unaffected signal, but is compromised by an increase of noise.
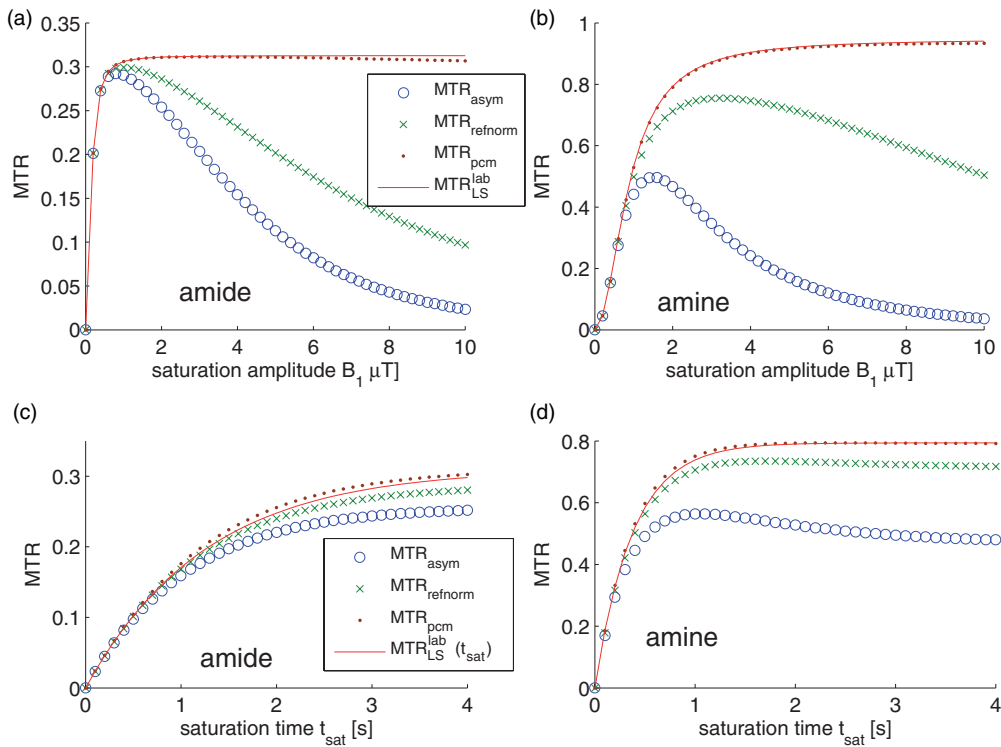
Figure 11. The ideal MTR in the large-shift limit approximation MTR_{FS}^{lab} (equation (35) and MTR calculated employing Z-spectra values on resonance and at the opposite frequency. MTR including concomitant direct water saturation is shown as a function of B_1 (a), (b) in steady-state and as a function of saturation time t_{sat} at $B_1 = 2~\mu T$ in transient-state (c), (d) at $B_0 = 7~T$. MTR_{asym} (equation (52)) is linked to the signal strength and increases with B_1, but decreases when spillover becomes important. Spillover dilution is stronger for amines (b) than for amides (a) owing to the smaller chemical shift. Therefore, without corrections, the interpretation of CEST effects is difficult. The first-order spillover correction $MTR_{refnorm}$ ((53)) compensates that slightly, while the second-order spillover correction MTR_{pcm} (54) yields almost the ideal effect $MTR_{FS}^{lab}(t)$ (equation (66)). In transient state the influence of spillover is more complicated exhibiting a biexponential behavior as a function of t_{sat} (equations (68) and (53)). Since the spillover effect increases with t_{sat}, for faster exchanging systems (e.g., amines (d)) an optimal saturation time (equation (69)) can exist where spillover is not yet fully effective. Parameters of example systems are given in the caption of figure 7.

MTR_{asym} is furthermore an important parameter, because it yields the actual signal strength of the CEST and MT effects. Experiments should therefore be performed around the maximum of MTR_{asym} where signal-to-noise ratio (SNR) is sufficient.

Another approach of spillover correction proposed by Sun *et al* (Sun and Sorensen 2008) employs additional R_1 and R_2 measurements. A spillover coefficient is defined to quantify the dilution (Sun and Sorensen 2008) in the MTR:

$$MTR = \frac{f_b k_b}{R_{1a} + f_b k_b} \cdot \alpha(1 - \sigma) \tag{56}$$

where α is the labeling efficiency from the weak-saturation-pulse approximation (compare equation (30) with p and q from equation (31)) (Zhou and Zijl 2006)

$$\alpha = \frac{\omega_1^2}{\omega_1^2 + pq + \frac{q}{p}\Delta\omega_b^2} \tag{57}$$

and σ the spillover coefficient obtained by the strong-saturation-pulse approximation (equation (32)) (Baguet and Roby 1997)

$$\sigma = 1 - \frac{r_{1a}}{k_{ab}} \left(\frac{R_{1a}r_{zb}\cos^2\theta + R_{1b}k_{ab}\cos\theta\cos^2(\theta/2)}{r_{za}r_{zb} - k_{ab}k_{ba}\cos^2(\theta/2)} - \frac{R_{1a}r_{2b}\cos^2\theta}{r_{za}r_{2b} - k_{ab}k_{ba}\sin^2\theta} \right). \tag{58}$$

In contrast to the spillover corrections based on the inverse metric, equations (53)–(55), this spillover coefficient needs input of T_1, T_2, and also exchange parameters. However, we think that this correction also takes the interference of the off-resonant R_{ex} with the on-resonant R_{ex} part into account (a-peak in equation (23)), which is not yet achieved by the equations (53)–(55).

As mentioned before, the ideal B_1 amplitude is affected by spillover. For the ratio MTR_{asym}, equation (52), Sun and Sorensen (Sun and Sorensen 2008, Sun *et al* 2005a) demonstrated that the optimal B_1 including spillover is given by

$$\omega_1 = \Delta\omega\sqrt{A} =$$
$$\sqrt{pq\left\{ \sqrt{1 + \frac{4(f_b+f_a)\bar{\beta}n_{2b}}{[f_b\eta_{2b}(1+2\bar{\beta}+\eta_b+4\eta_a)+f_a(4+4\beta^2+\eta_{2b}(5+\eta_{2b}+8\eta_a)-4\beta(2+\eta_{2b}+\eta_{2b}\eta_a))]}\frac{\Delta\omega^2}{pq}} - 1 \right\}}, \tag{59}$$

where p, q are given in equation (31) and

$$\text{where} \quad \beta = \frac{k_{ab}k_{ba}}{r_{1a}r_{1b}}, \bar{\beta} = 1 - \beta, \eta_a = \frac{r_a}{r_{1a}}, \eta_b = \frac{r_b}{r_{1b}}, \eta_{2b} = \frac{r_{2b}}{r_{1b}},$$
$$r_a = r_{2a} - r_{1a}, r_b = r_{2b} - r_{1b}, \eta_{2b} = \frac{r_{2b}}{r_{1b}}, f_a = \frac{R_{1a}}{r_{1a}},$$
$$\text{and} \quad f_b = \frac{R_{1b}}{k_{ba}}. \tag{60}$$

Jin *et al* derived a more simple formula for the case of optimization of MTR_{asym} of a two-pool system (Jin and Kim 2013b):

$$\omega_{1,opt} \approx k_b \sqrt{\sqrt{\frac{R_{1a}}{2R_{2a}}} + \frac{k_b}{\delta\omega_b} + \frac{k_b^2}{\delta\omega_b^2}\sqrt{\frac{R_{2a}}{2R_{1a}}}}. \tag{61}$$

This multi-parametric dependence of the optimal B_1 is the reason why for a specific CEST effect in tissue, B_1 must always be explored and optimized *in vivo*.

4.5. Reference value

The critical quantity for all conventional evaluations of MTR is the reference value Z_{ref}. The often used reference at the opposite frequency $Z_{ref} = Z(\Delta\omega_{ref} = -\Delta\omega)$ leads to reliable results only if

- The reference frequency is exactly measured at the opposite frequency of the label scan.
- There are no interfering pools at the reference frequency, like NOE, CEST or asymmetric MT effects.
- $R_{ex}(\Delta\omega)$ is negligible at the reference frequency.

Although all three criteria may be violated *in vivo*, asymmetric approaches were used in many applications. After correction of B_0 errors (section 4.9), the implicit assumption for the obtained contrast is that the competing effects are either negligible or constant within the region of interest.

For clinical applications of CEST it may be practical to dispose of a new contrast mechanism without the knowledge of the dominant underlying mechanism. In this line, many

asymmetric approaches are applied even to systems where NOEs or asymmetric MT effects are present. Examples are gagCEST (Ling *et al* 2008, Singh *et al* 2011) and APT (Gerigk *et al* 2012, Jia *et al* 2011, Jones *et al* 2006, Zhou 2011). From a theoretical point of view for all asymmetric approaches it has to be verified that this implicit assumption about competing effects is valid. Only then an insight into the origin of the observed effect and the extraction of specific parameters will be reliable. For example, the APT (+3.5 ppm)-weighted imaging contrast (Zhou *et al* 2003, 2011) is presently under discussion concerning the influence of NOE effects at –3.5 ppm (Jin *et al* 2012b, Liu *et al* 2013c, Zhou *et al* 2012). The interactions of multiple-pool systems are discussed in the following section (section 4.6). Recently, methods for APT imaging with improved reference value were reported such as clean-APT (Xu *et al* 2013a) and MTR_{double} (Zu *et al* 2012). These approaches are favorable for the interpretation of the origins of CEST effects. MTR_{double} obtains a reference value by means of pulsed saturation by using a $360°$ pulse as reference for a $180°$ pulse. The power can be chosen in a way that direct effects are the same for both pulses, while exchange effects depend strongly on the flip angle. This method is discussed in section 6 ('MTR_{double}'). Similarly, a reference scan can be obtained by a pulse train with the same pulse width and power, but different delay time. Employing a variable-delay multi-pulse train Xu *et al* showed that for slowly exchanging APT and NOE a good reference can be obtained if the delay time is increased from 0.7 (label scan) to 110 ms (reference scan) (Xu *et al* 2013a).

Another method to obtain a reference value is by fitting the direct water saturation as suggested in Dula *et al* (2012) and Jones *et al* (2012). This approach is advantageous since no effects from the opposite side are subtracted, but it relies on what is interpreted as direct water saturation by the fit. Since also R_{ex} has an on-resonant part (equation (23)), the $R_{ex,ref}$ of this reference would be interpreted as direct water saturation. Both fit and asymmetric analysis are affected by R_{ex}^{ref} leading to an apparent $R_{ex,app}$ which is given by

$$R_{ex,app} = R_{ex}^{lab} - R_{ex}^{ref}. \tag{62}$$

4.6. Multiple pool systems

When exchange processes are studied in living tissue, many different pools are effective and contribute to the Z-spectrum (figure 3). This complication was addressed in e.g. Jin *et al* (2012b), Li *et al* (2008), Liu *et al* (2013c) and Zhou and Zijl (2006).

We consider a system of three pools, which is characterized by direct saturation (pool a), exchange-dependent relaxation of pool b, and an additional pool c. Pools b and c can be, e.g., the amide and amine pools, but also exchange-relayed NOEs or, as shown in Zaiss and Bachert (2012a), a shifted semi-solid MT pool.

Trott and Palmer (2004) showed that under the assumption of a small back exchange rate and no exchange between the pools b and c, the corresponding relaxation rates in the rotating frame of direct saturation and exchange with pools b and c add up to the global rate $R_{1\rho}$:

$$R_{1\rho} = R_{eff} + R_{ex,b} + R_{ex,c}. \tag{63}$$

This approach was proven numerically by Zaiss and Bachert (2012a) to be able to describe multiple-pool BM systems (figure 8). Since $R_{1\rho}$ appears in the denominator of the steady-state solution Z (equation (19)), the effects in the Z-spectrum add reciprocally, analogous to electric resistors in a parallel circuit (figure 12):

$$1/Z = 1/Z_{water} + 1/Z_b + 1/Z_c. \tag{64}$$

Signal addition in MRS and MRZS

$$S_{\text{total}} = S_{\text{water}} + S_{\text{pool b}} + S_{\text{pool c}}$$

$$1/S_{\text{total}} = 1/S_{\text{water}} + 1/S_{\text{pool b}} + 1/S_{\text{pool c}}$$
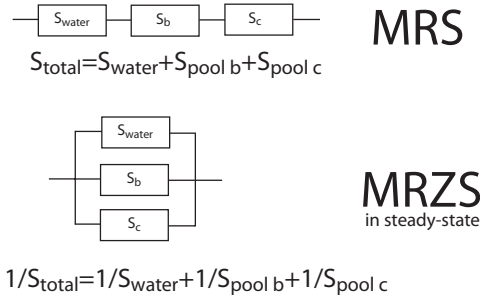
Figure 12. The complex resonance signals of the different compounds detectable with NMR spectroscopy (MRS) sum up, whereas the effects in steady-state MR Z-spectroscopy (MRZS) sum up reciprocally. At simultaneous occurrence the diverse effects behave like resistors in a serial electrical circuit in the case of MRS and like resistors in a parallel circuit in MRZS. Dilution of effects can be understood and appropriately compensated by this 'inverse metric'.

Under the assumption $R_{\text{ex}} \ll R_{\text{eff}}$ or, for large shifts, $k_{\text{a}} \ll R_{1\text{a}}$ which means small CEST effects, a direct superposition is still valid owing to the relation

$$Z = \frac{R_{1\text{res}} P_z}{R_{\text{eff}} + R_{\text{ex,b}} + R_{\text{ex,c}}} \approx \underbrace{\frac{R_{1\text{res}} P_z}{R_{\text{eff}}}}_{1 - \frac{R_2 \omega_1^2}{R_1 \Delta\omega_{\text{a}}^2 + R_2 \omega_1^2}} - \frac{R_{1\text{res}} P_z}{R_{\text{eff}}^2} R_{\text{ex,b}} - \frac{R_{1\text{res}} P_z}{R_{\text{eff}}^2} R_{\text{ex,c}}$$

$$\overset{\text{LS}}{\approx} 1 - \frac{R_2 \omega_1^2}{R_1 \Delta\omega_{\text{a}}^2 + R_2 \omega_1^2} - \frac{R_{\text{ex,b}}}{R_{1\text{a}}} - \frac{R_{\text{ex,c}}}{R_{1\text{a}}}. \tag{65}$$

The first term is a Lorentzian line of the direct water saturation (equation (29)). As R_{ex} is also approximately a Lorentzian line (equation (25)), equation (65) explains why approaches that employ a superposition of Lorentzians to model CEST effects are successful (Desmond *et al* 2013, Zaiss *et al* 2011).

4.7. Transient CEST effect and spillover

As discussed above (section 3.3), for the description of the transient-state the full solution of the BM equations must be considered. Including the time dependence one obtains in the large-shift limit an extension of (36), namely ($Z_i = 1$):

$$\text{MTR}_{\text{LS}}(\Delta\omega, t_{\text{sat}}) = 1 - Z(\Delta\omega, t_{\text{sat}}) = \frac{R_{\text{ex,LS}}(\Delta\omega)}{R_{1\text{a}} + R_{\text{ex,LS}}(\Delta\omega)} \cdot (1 - e^{-(R_{1\text{a}} + R_{\text{ex,LS}}(\Delta\omega))t_{\text{sat}}}). \tag{66}$$

For the label scan we obtain

$$\text{MTR}_{\text{LS}}^{\text{lab}}(t_{\text{sat}}) = \frac{k_{\text{a}} \cdot \alpha}{R_{1\text{a}} + k_{\text{a}} \cdot \alpha}(1 - e^{-(R_{1\text{a}} + k_{\text{a}} \cdot \alpha)t}). \tag{67}$$

Important to note is that α also appears in the exponent.

When initial magnetization and spillover terms are included the monoexponential MTR (66) becomes a biexponential function (figure 11(d)):

$$\text{MTR}_{\text{asym}}(\Delta\omega, t_{\text{sat}}) = \text{MTR}_{\text{asym}}^{\text{ss}}(\Delta\omega) + (P_{z\,\text{eff}} P_z Z_i - Z_{\text{ref}}^{\text{ss}})\, e^{-R_{1\rho}(\Delta\omega_{\text{ref}})t_{\text{sat}}}$$
$$- (P_{z\,\text{eff}} P_z Z_i - Z_{\text{lab}}^{\text{ss}})\, e^{-R_{1\rho}(\Delta\omega_{\text{lab}})t_{\text{sat}}}. \tag{68}$$
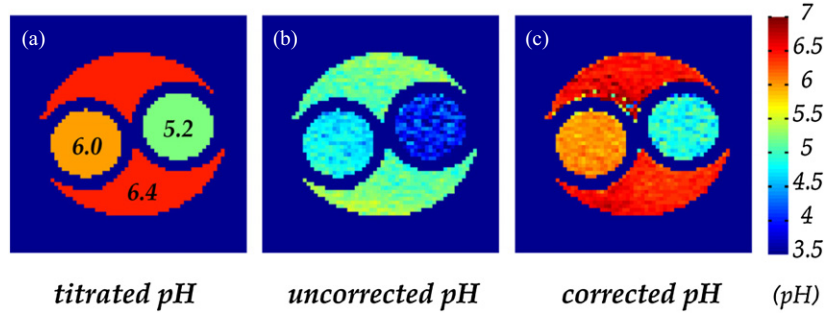
Figure 13. CEST imaging of creatine in aqueous solution enables absolute quantification of pH. However, without the correction of spillover and labeling exchange rates, pH values are underestimated due to the spillover dilution of the CEST effect.

As a consequence, MTR_{asym} can have a maximum as a function of saturation time (figure 11(d)), which is determined by direct saturation. Jin *et al* (2012a) found for SL that for slow exchange $t_{sat} = \infty$ is optimal, while for intermediate exchange the optimal saturation time is

$$t_{sat,opt} = \frac{1}{\sin^2\theta \cdot R_{2a} + R_{ex}}. \tag{69}$$

This parameter depends on B_1, exchange and water pool properties and is therefore often optimized experimentally.

If instead of $MTR_{asym}(t_{sat})$ an exponential fit in t_{sat} at the offset of interest (Z_{lab}) and the reference (Z_{ref}) is performed, one obtains—similar to SL experiments—$R_{1\rho}(\Delta\omega)$ and $R_{eff}(\Delta\omega)$. These rates can be used to isolate R_{ex} which then yields a spillover correction. If the steady-state is measured directly one can evaluate $R_{1\rho}$ via the following rearranging first proposed by Sun (2012) and extended by Zaiss and Bachert (2012a):

$$\tilde{Z}(\Delta\omega, t_{sat}) = \frac{Z(\Delta\omega, t_{sat}) - Z^{ss}(\Delta\omega)}{P_z P_{z\,eff} - Z^{ss}(\Delta\omega)} = e^{-R_{1\rho}(\Delta\omega) \cdot t_{sat}}. \tag{70}$$

With a reference scan without exchange-dependent relaxation again R_{ex} can be isolated. This method was called 'QUantification of Exchange by Saturation Time with Ratiometric Analysis' (QUESTRA (Sun 2012)):

$$QUESTRA_{Rex} = \frac{\tilde{Z}(\Delta\omega_{lab}, t_{sat})}{\tilde{Z}(\Delta\omega_{ref}, t_{sat})} = e^{-R_{ex}^{lab} \cdot t_{sat}}. \tag{71}$$

It is important to note that with transient methods R_{ex} can be determined directly. By steady-state evaluation only the ratio R_{ex}/R_1 is obtained (equation (55)). For further discussion of transient methods, see section 6.

4.8. Pulsed saturation

As mentioned in section 2, MRZS experiments at clinical MRI systems are restricted because large pulse durations are excluded for reasons of safety. Therefore, series of pulses must be used for preparation before readout. For modeling of Z-spectra that are obtained in saturation experiments where series or 'trains' of short pulses are applied to saturate the spin system of the solute the sole exact solution arises from the full numerical integration of the BM equations. Numerical integration was discussed in section 3.2; it can be extended to arbitrary
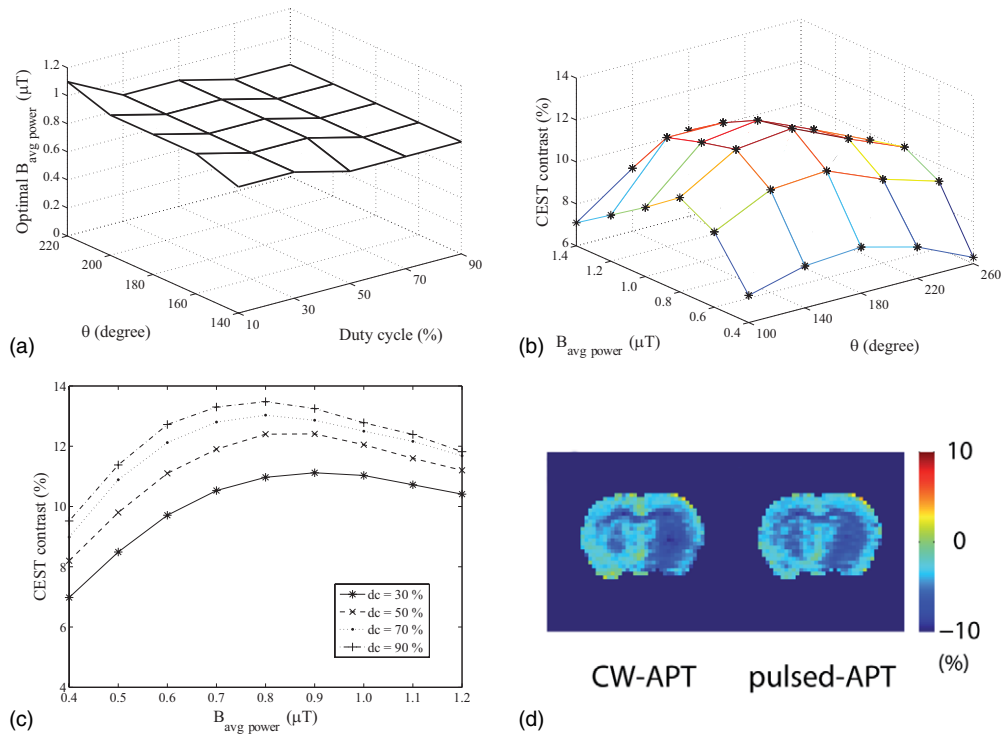
Figure 14. The 'orthogonal' basis of pulsed CEST. The average power B_{1cwpe}, duty-cycle (DC) and the flip angle can be optimized separately. For slowly exchanging systems, such as APT, the optimum values are flip angles around $180°$, $B_{1cwpe} \approx 1$ μT and maximum DC. Similar findings were reported by Sun *et al* (2011) who also showed that cw CEST and pulsed CEST yield similar APT contrast in acute ischemia in the rat brain (d). Reproduced with kind permission from ((a)–(c)) Zu *et al* (2011b), copyright © 2011 John Wiley & Sons Ltd., and (d) Sun *et al* (2011), copyright © 2011 John Wiley & Sons Ltd..

pulse shapes by step-wise calculation. Numerical simulations of pulsed Z-spectra are time-consuming, but provide insight into the saturation process. They also provide the model of minimal approximation and thus a reference for analytical models (Portnoy and Stanisz 2007).

However, there also exist approximate analytical solutions; two of them we will discuss now.

The first approach models pulse-saturation properties in the course of a cw experiment using a cw power equivalent B_{1cwpe} defined by

$$B_{1cwpe} = \sqrt{\frac{1}{t_p + t_d} \int_0^{t_p+t_d} B_1^2(t)\, \mathrm{d}t}. \tag{72}$$

It turned out (Sun *et al* 2011, Zu *et al* 2011b) that B_{1cwpe} is the appropriate B_1 norm to obtain similar behavior of labeling and spillover as in a cw experiment and thus similar optimal B_1 (figure 14(c)).

Zu *et al* (2011b) showed that using the cw power equivalent the experimental parameters B_{1cwpe}, duty-cycle (DC) and flip angle can be optimized separately (figures 14(a)–(c)). Employing B_{1cwpe} (Tee *et al* 2012) showed that the cw solution (equations (16) or (18)), is also suitable to model pulsed CEST with Gaussian-shaped inversion pulses for exchange rates up to 50 s^{-1} properly.

The second analytical approach was developed by Santyr *et al* (1994) for trains of SL pulses. However, due to the equivalence of SL and CEST (Jin and Kim 2012, Yuan *et al* 2012, Zaiss and Bachert 2012b) this approach is also applicable to pulsed CEST, especially for the case of intermediate exchange where rotations during the pulse and biexponetial behavior during the pause are negligible (Roeloffs *et al* 2013). This approach is based on an interleaved-pulse-pause modeling assuming relaxation with rate $R_{1\rho}$ during the pulse duration t_p and R_{1a} relaxation during the interpulse delay t_d. Santyr's approach is similar to that of Sled and Pike (2000) for MT which basically describes pulsed MT by interleaving the solution of free precession and cw irradiation. Here B_1 is the amplitude of the SL saturation pulse and the dependence of the Z-value on t_p and t_d is explicitly given. Expressing equation (A4) in Santyr *et al* (1994) in our notation yields Z_n, the Z-spectrum obtained upon irradiation of a train of n saturation pulses with duration $t_{sat} = n(t_p + t_d)$:

$$Z_n = (Z_i - Z^{SSP}) \, e^{-R_{1\rho}^{pulsed} t_{sat}} + Z^{SSP}. \tag{73}$$

Here Z_i is the initial Z-value, Z^{SSP} is the steady-state-pulsed value,

$$Z^{SSP}(\Delta\omega) = 1 - \frac{(1 - e^{R_{1\rho}(\Delta\omega)t_p})\left(1 - \frac{R_{1a}\cdot\cos\theta}{R_{1\rho}(\Delta\omega)}\right)}{1 - e^{R_{1\rho}^{pulsed}(\Delta\omega)(t_p + t_d)}} \tag{74}$$

and

$$R_{1\rho}^{pulsed}(\Delta\omega) = R_{1\rho}(\Delta\omega) \cdot DC + R_{1a} \cdot (1 - DC). \tag{75}$$

Assuming small arguments of the exponential terms, equation (74) can be approximated by (Zaiss *et al* 2013a)

$$Z^{SSP}(\Delta\omega) = \frac{R_{1a}(\cos\theta \cdot DC + (1 - DC))}{R_{1\rho}^{pulsed}(\Delta\omega)}. \tag{76}$$

This expression for Z^{SSP} is similar to the cw formula for SL, but includes the pulse-train parameter duty-cycle DC and hence pulse duration t_p and interpulse delay t_d explicitly. However, any rotation of the magnetization of pool b and any transfer of magnetization during t_d is neglected in this approach. This leads to deviations of MTR for short pulses or small exchange rates if the model is not extended appropriately (Roeloffs *et al* 2013).

We expect that the pulse shape can be treated in a similar manner as the integration of adiabatic SL pulses (Mangia *et al* 2009, Michaeli *et al* 2006). Accordingly, the time-average of the relaxation rate $R_{1\rho}$

$$\overline{R}_{1\rho}(\Delta\omega) = \frac{1}{t_p} \int_0^{t_p} R_{1\rho}(\Delta\omega, \omega_1(t)) \, dt \tag{77}$$

was proposed. However, due to the short pulses further eigenvalues related to $T_{2\rho}$ and also complex eigenvalues must be taken into account (Mangia *et al* 2009, Murase 2012, Zaiss and Bachert 2012a).

4.9. Artifacts—fat, B_0, B_1

Lipids. Several artifacts specific for MRZS can lead to serious misinterpretation of Z-spectra data. Most important are direct effects of other proton species, e.g. those in mobile lipids (fatty acids, triacylgylcerides). Hence, if 'fat saturation' is omitted before readout, direct saturation of protons in fatty acids can be misinterpreted as transfer effect (Schmitt *et al* 2011b). This artifact can be counteracted by selective fat saturation before readout (Dula *et al* 2012, Sun *et al* 2005b) or partially reduced by tissue segmentation (Liu *et al* 2013a).

B₀ correction. The second significant sources of errors are inhomogeneities of B_0 and B_1 fields. B_0 is crucial, in particular when asymmetric evaluation approaches are applied. When the position of the symmetry axis slightly deviates from the center of the water peak, direct water saturation is interpreted as CEST effect especially near the water resonance (Singh *et al* 2011). To compensate this artifact, more than two offsets in the *Z*-spectrum must be acquired and an additional B_0 field map. Using this field map the *Z*-spectrum data can be interpolated and registered pixel-by-pixel in the frequency dimension. The water shift referencing method (WASSR, (Kim *et al* 2009)) is a useful method for B_0 field mapping: a low-power pulse ($B_1 = 0.25 \, \mu$T, $t_p = 100$ ms) is applied to obtain *Z*-spectra upon direct water saturation sampled around the water resonance (–1 to +1 ppm). The minimum or the offset with minimum asymmetry yields the water proton shift. This is a time-consuming method compared to direct field mapping, but evaluation is straightforward and the actual CEST sequence can be used to acquire the B_0 map. To obtain a B_0 map without additional scanning time, the interpolation of *Z*-spectra data (Zhou *et al* 2003) or fit of direct water saturation (Dula *et al* 2012, Jones *et al* 2012, Zaiss *et al* 2011) were reported to enable appropriate B_0 correction. Less B_0-sensitive approaches were also reported, see section 6 for methods as SAFARI introduced by Scheidegger *et al* (2011) or the MTR$_{\text{double}}$ method of Zu *et al* (2012).

To correct a two-point analysis affected by B_0 and B_1 inhomogeneities, Sun *et al* (2007a) provided a correction algorithm which is able to compensate B_0 shifts up to ± 0.5 ppm. The algorithm requires estimations of system parameters like relaxation and exchange rates.

B₁ correction. Sections 4.1 and 4.2 showed that CEST and NOE contrast strongly depend on B_1. Hence inhomogeneities of the B_1 field will compromise the CEST contrast. First approaches to correct artifacts resulting from B_1 inhomogeneities were performed by Sun *et al* (2007a) and Singh *et al* (2012); these methods require additional information either on system parameters or *Z*-values for different B_1. We will outline in the next section that B_1 correction and quantification are related and quantification can be performed by means of variation of B_1. If changes of CEST effects are reported, at least a B_1 field map should be provided to prove that these are not caused by deviations in B_1.

5. Quantification of *Z*-spectra data—from MTR to exchange rate and concentration

In section 3.3, we showed that the *Z*-spectrum is the dynamic solution for the normalized *z*-component of the magnetization which obeys in the effective frame a monoexponential decay law with time constant $T_{1\rho}$ towards a reciprocal sum of functions R_{eff} and R_{ex} with Lorentzian line shapes. Thus, the only parameters that can be directly accessed by the evaluation of *Z*-spectra are the decay rate $R_{1\rho}$—which again is a sum of Lorentzian-shaped functions— and line width and amplitude of these Lorentzians. Even if some of these Lorentzians can be isolated by an appropriate MTR or calculated employing relaxation data from additional measurements, the determination of underlying parameters requires a series of measurements with different irradiation parameters which change the width and amplitude of the Lorentzian functions. The known behavior of these changes can then be utilized to extract intrinsic parameters if peaks can be described by a single pool. The most important example is probably QUESP which stands for QUantification of Exchange by Saturation Power (McMahon *et al* 2006). Since the amplitude $R_{\text{ex}}^{\text{lab}}$ (equation (26)) and the width Γ of R_{ex} (equation (24)) in the large-shift limit (Zaiss and Bachert 2012a) are linear functions of ω_1^2:

$$1/R_{\text{ex}}^{\text{max}} = \frac{k_b + R_{2b}}{f_b} \omega_1^{-2} + \frac{1}{f_b k_b} \tag{78}$$

and

$$\frac{\Gamma^2}{4} = \frac{k_b + R_{2b}}{k_b}\omega_1^2 + (k_b + R_{2b})^2, \tag{79}$$

experiments that measure CEST effects as a function of ω_1^2 yield the needed constant and linear coefficients in equations (78) and (79).

In general, both the amplitude R_{ex}^{lab} and width Γ are mandatory to determine k_b, f_b and R_{2b} separately by QUESP. However, for many cases where R_{2b} is either known or negligible compared to k_b, QUESP may yield k_b and f_b from either the amplitude or the width of the CEST effect.

Under the assumption of negligible direct saturation and $R_{2b} \ll k_b$, which is valid for PARACEST, the following ratio introduced by Dixon *et al* (2010b) also yields k_b independently of f_b if several values for ω_1^2 are employed:

$$\text{MTR}/(1 - \text{MTR}) = T_{1a}f_b\left(\frac{1}{k_b^2} + \frac{1}{\omega_1^2}\right). \tag{80}$$

Under similar assumptions, the separation of k_b and f_b is also feasible by means of the original QUESP formula (McMahon *et al* 2006).

For transient-state methods, the initial approach QUantification of Exchange by Saturation Time (QUEST, (McMahon *et al* 2006)) was extended by a 'ratiometric analysis' (QUESTRA) (section 4.5) and by the inclusion of the projection factors and the full eigenvalue (QUESTRA$_{Rex}$, equation (71)). Since the apparent relaxation rate is always $R_{1\rho}$ in a QUEST experiment at one single B_1 amplitude, we conclude that only R_{ex} can be obtained by this approach and not—in contrast to QUESP—f_b and k_b separately.

The width Γ measured for different rf amplitudes B_1 can also be used to quantify the system if R_{2b} is known or can be assumed to be small (Jin *et al* 2011, McVicar *et al* 2012).

Often a T_1-map is needed to obtain a proper evaluation of CEST effects, because T_1 scales all effects in the Z-spectrum. It is important to note that R_{1a} is not necessarily the $R_{1,obs}$ measured in an inversion recovery experiment. As stated for MT in Henkelman *et al* (1993) and Sled and Pike (2000), $R_{1,obs}$ is the smaller one of the two eigenvalues of the system in the absence of irradiation. The relation of R_{1a} and $R_{1,obs}$ in the case of a two-pool system is

$$R_{1a} = \frac{R_{1,obs}}{1 + \left(\frac{\frac{k_a}{R_{1a}}(R_{1b}-R_{1,obs})}{(R_{1b}-R_{1,obs})+k_b}\right)}. \tag{81}$$

For $k_a \ll R_{1a}$ the observed $R_{1,obs}$ and R_{1a} can be assumed to be approximately equal. For larger k_a this deviation of measured and theoretically required R_1 has to be taken into account for quantification. Desmond and Stanisz showed how to calculate $R_{1,obs}$ for a system that exhibits CEST and MT effects (Desmond and Stanisz 2012).

There are further procedures for the quantification of Z-spectra, especially for the pulsed saturation case which offer more degrees of freedom and allow filtering by exchange rate or relaxation time. This is of special interest *in vivo*, as the simple two-pool assumption is not valid. Since these approaches depend on the applied experimental method, we discuss them in the following section.

6. Methods and pulse sequences

For the estimation of the significance of an observed CEST effect or method we think the following issues have to be considered. The treatment of B_0 inhomogeneities and B_0 errors and their dependence on the employed *reference value* is of central importance

and must be considered carefully. Furthermore, it has to be shown that the reference value does not contain significant concomitant contributions. If not acquired in fully relaxed state, the *normalization scan M_0* must be demonstrated to be appropriate. As discussed in section 4.4, the interference with the water peak (*spillover*) and MT must be assessed and if possible *spillover* and T_1 corrections must be performed. Otherwise at least T_1 and T_2 maps should be provided for comparison as well as data on the interfering semi-solid macromolecular MT. In addition, MRZS data can be corrected for B_1 inhomogeneities using B_1 field maps, at least such a map allows the discussion of contrast changes due to labeling issues (section 4.1). For the correlation of phantom and *in vivo* results the dependence of exchange effects on temperature, pH, buffer and viscosity should be investigated. It has to be discussed whether the employed method or assumptions allow to interpret changes in CEST and NOE peaks as alterations in concentrations, exchange rates or cross-relaxation rates. For applications of CEST in clinical studies scanning time, SAR, and SNR of small effects must be considered. Finally, in cases where the criteria for the unequivocal identification of CEST peaks/effects are compromised, but also for systems with strong spillover effect, control measurements at higher B_0 recommended.

Continuous-wave CEST and spinlock. The principal concept of CEST requires that saturation is generated by cw irradiation (cw-CEST). It was shown that cw-CEST and off-resonant SL are equivalent experiments (Jin *et al* 2011, 2012a, Yuan *et al* 2012, Zaiss and Bachert 2012a, 2012b). In general, SL yields larger SNR than cw-CEST—the enhancement factor is $1/\cos\theta$ in steady-state and up to $1/\cos^2\theta$ in transient-state (projection factors in equations (18) and (19)). Moreover SL suppresses oscillations of the transverse magnetization of water protons which distort the cw-CEST signal especially for short irradiation times (Murase 2012, Zaiss and Bachert 2012a). On the other hand, CEST Z-spectra can be B_0-corrected by post-processing (Kim *et al* 2009) in contrast to SL Z-spectra. Artifacts in the latter can be reduced by using adiabatic SL pulses (Santyr *et al* 1994). Thus, steady-state cw-CEST and SL may have the best labeling efficiency and also a high selectivity, but generally cannot be applied to clinical MR scanners due to SAR restrictions of pulse width. However, by means of two interleaved pulse trains and parallel transmit technique it may be possible to achieve effective cw-saturation within common scanner limitations (Togao *et al* 2012).

In vitro, scan time can be reduced significantly if one spatial dimension is employed for spectral encoding. This ultra-fast-Z-spectroscopy (UFZ, (Xu *et al* 2013b)) applies a gradient during irradiation to saturate at different spatial positions with different frequency offsets. The same gradient applied during readout maps the spatial position back to the frequency axis (figure 15). With one reference scan a complete Z-spectrum is obtained by two scans altogether. UFZ-spectra may be affected by simultaneous apparent diffusion processes in encoding direction; if this becomes dominant, BM theory will not be able to describe UFZ-spectra.

Pulsed CEST—saturation regime. Pulsed methods with relatively long pulses where MT mainly occurs during rf irradiation are similar to cw-CEST or SL. We call the regime where $t_p > 1/k$ 'saturation regime'. Here, $R_{1\rho}$, the eigenvalue during irradiation, governs the system during each pulse and apparent rotation effects will vanish (figure 16) or do not contribute significantly during the interpulse delay. The effects of shorter pulses ($t_p \leqslant 1/k$) are discussed below ('rotation regime').

SAR restrictions of clinical systems call for pulsed-saturation techniques. One consequence is a larger set of saturation parameters: number of pulses, pulse width, interpulse
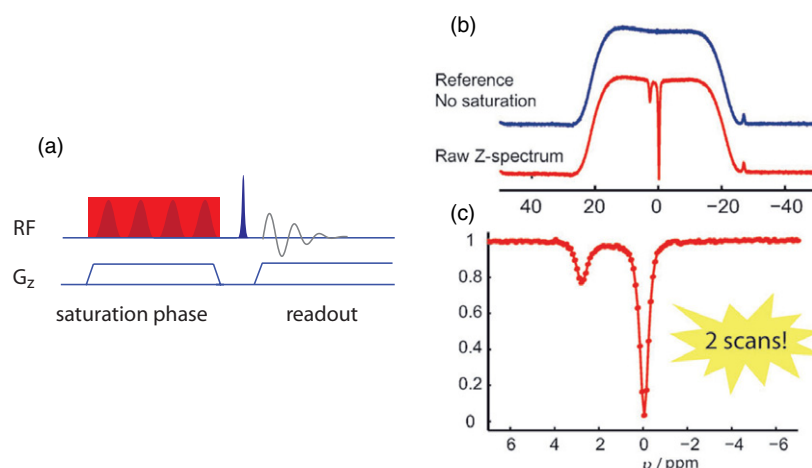
Figure 15. Ultra-fast-Z-spectroscopy. (a) By application of a gradient in *z*-direction, different frequency offsets are spatially distributed and can be encoded by the same gradient during readout. Isotropy in one dimension allows a strong reduction of the scan time—a *Z*-spectrum (c) can be obtained in two shots (b) (Xu *et al* 2013b). (b) and (c) reproduced with kind permission from Xu *et al* (2013b), copyright © 2013 John Wiley & Sons Ltd..
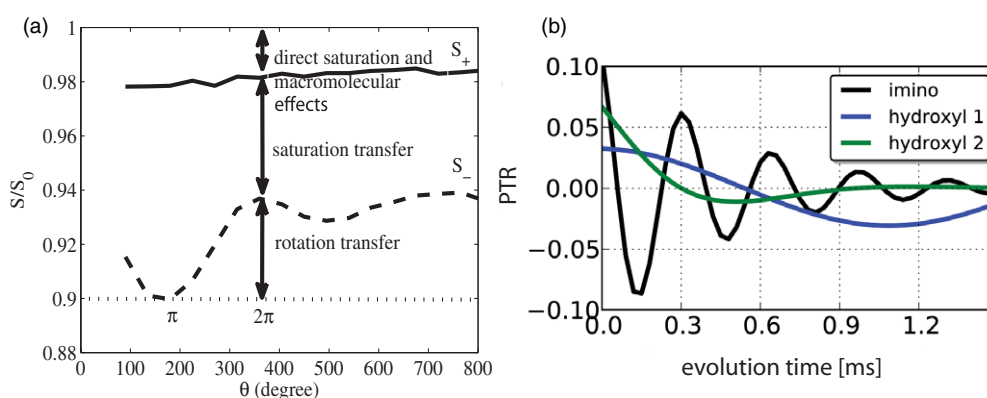

Figure 16. Upon transition from cw irradiation to trains of short pulses, rotation effects of the magnetizations of the exchanging pools can be induced. (a) CERT induces oscillations by selective pulses with definite flip angles. Rotations induced by non-selective 90° pulses and subsequent free evolution in the transverse plane allows FLEX (Yadav *et al* 2012). (b) The signal of FLEX, i.e. the PTR as a function of the evolution time, shows the superposition of oscillations of the magnetizations of imino and hydroxyl protons which can be separated by Fourier decomposition. Reproduced with kind permission from (a) Zu *et al* (2012), copyright © 2012 John Wiley & Sons Ltd., and (b) Yadav *et al* (2012), copyright © 2012 John Wiley & Sons Ltd..

delay time, power and pulse shape. The pulse shape is of particular importance since it determines the selectivity of saturation, whereas changes in the first four parameters have similar effects as cw saturation. Commonly used pulse shapes in CEST experiments are Gaussian (Schmitt *et al* 2011a), Hanning–windowed Gaussian (Desmond and Stanisz 2012), e-burp (Aime *et al* 2002) or Fermi (Dixon *et al* 2010a). Off-resonant SL pulses and adiabatic SL pulses (Santyr *et al* 1994) are other useful pulse shapes for CEST experiments, which also reduce rotation effects of the water peak. Smooth saturation profiles of shaped pulses arise

from their adiabaticity (Zu *et al* 2012). The aim is to obtain high labeling of the CEST pool, high residual R_{1a}, but low direct saturation of water. Presently there is—to our knowledge—no quantitative comparison of the benefits and disadvantages of different pulse shapes applied so far to CEST studies. An assessment of the influence of rf pulse shapes on Z-spectra is given in the recent review of Liu *et al* (2013b).

Pulsed CEST—rotation regime. For $t_p \leqslant 1/k$ it is favorable to subdivide the saturation pulse train in 'label-transfer modules' (Friedman *et al* 2010, van Zijl and Yadav 2011). The label modules (duration t_p) are typically short and induce a change of the magnetizations of pools a and b by the rotation of the magnetization of pool b. We call this regime 'rotation regime'. This state is balanced during the transfer module or interpulse delay time t_d. The efficiency of labeling is determined by the decay of the magnetization of pool b during the pulse which runs off with $\approx \exp(-[k_{sw} + R_{2b}]t_p)$. Hence t_p must be shorter than $1/(k_b + R_{2b})$ to yield an effective rotation. This condition can be used as a k_b- and T_2-filter (Xu *et al* 2013a, Zu *et al* 2012).

Two approaches directly use these rotations of the magnetization for labeling the CEST pool: chemical exchange rotation transfer (CERT) and frequency-labeled exchange (FLEX) (figure 16). With CERT this labeling is achieved via rotation of the CEST pool magnetization vector by means of a selective rf pulse. In FLEX, the rotation is induced after a non-selective rf pulse using different free-precession frequencies (figure 16). While CERT yields Z-spectra, FLEX requires Fourier transformation to obtain a 'Z-spectrum'.

A straightforward, but effective CERT approach is inversion transfer. The selectivity of short saturation pulses decreases significantly which makes the choice of the pulse shape important. Reported inversion pulses are e.g. Gaussian (Zhou *et al* 2003), Blackman-shaped (Scheidegger *et al* 2011) or d-SNOB pulses (Meldrum *et al* 2011). Nevertheless, it was shown that if $t_p < 1/k_b$, inversion transfer is up to two times more effective than saturation transfer and nearly the efficiency of cw irradiation can be achieved (Sun *et al* 2011, Zu *et al* 2011b). Tee *et al* (2012) showed that inversion transfer for $k_b < 50$ s^{-1} can be modeled by the cw solution of the BM equations employing the cw power equivalent B_{1cwpe} (equation (72)).

A particularly interesting CERT approach, namely MTR$_{double}$ (Zu *et al* 2012), employs saturation by a series of inversion pulses and for reference saturation with a series of $360°$ pulses:

$$\text{MTR}_{\text{double}} = Z(360°) - Z(180°). \tag{82}$$

Due to the subtraction this method suffers from signal loss in comparison to MTR$_{asym}$ of inversion transfer. However, the big benefit is that B_0 inhomogeneities have much less influence than in the asymmetry analysis, since the reference value is obtained at the same offset. Also, effects at the opposite frequency do not compromise MTR$_{double}$. The basic idea is that by keeping the power constant and varying only the flip angle, the direct saturation effects are the same, but the exchange effects are altered. However, this approach requires that the employed rf pulse moves the water magnetization adiabatically and is simultaneously able to invert the magnetization of the exchanging pool effectively. These conditions can be fulfilled only for slowly exchanging systems such as amide proton transfer (APT) or NOEs or large frequency offsets due to the chemical shift or field strength B_0. For the multi-angle ratiometric CERT, three different rotations with flip angles $\theta = 180°$, $360°$ and $540°$ were employed (Zu *et al* 2011a). This method again needs an asymmetry evaluation, but enables direct access to the exchange rate k_b.

Variable-delay multi-pulse approach. Another direct method to obtain the exchange rate k_b was proposed by Jones *et al* (2013) and Xu *et al* (2013a). They used trains of pulses with
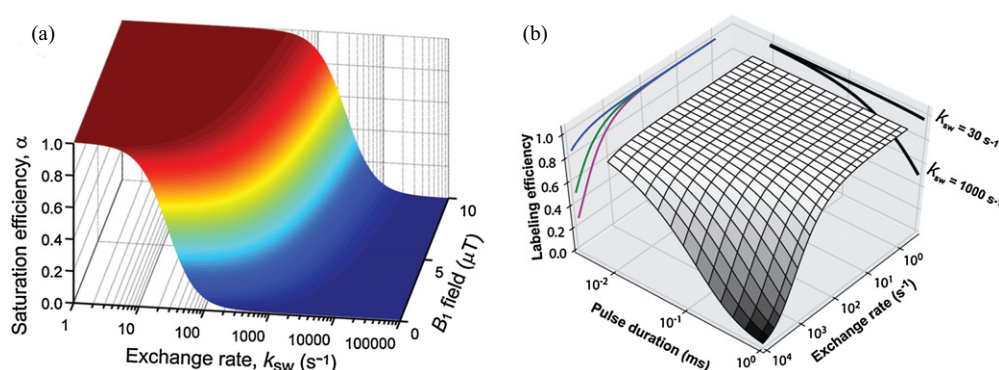
Figure 17. Labeling efficiencies (section 4.1) for (a) CEST (equation (42)) and (b) FLEX (factor λ in Yadav *et al* (2012). While CEST is limited by the maximum B_1 amplitude, FLEX is limited by the minimal pulse duration. CEST labeling efficiency shows a rapid decrease for $k_b = k_{SW} > 1000 \text{ s}^{-1}$, whereas FLEX has still a fairly good labeling even of pools with exchange rates up to 10 000 s^{-1} (projections on the left are curves for pulse durations of 0.02, 0.1 and 0.2 ms, respectively). Reproduced with kind permission from (a) Van Zijl and Yadav (2011), copyright © 2011 John Wiley & Sons Ltd., and (b) Yadav *et al* (2012), copyright © 2012 John Wiley & Sons Ltd..

fixed length and flip angle 180°, but variable delay time between the pulses. Implicitly, the biexponential decay during the pulse pause is utilized which becomes important for slowly exchanging pools such as APT and dipolar-coupled systems (NOE). Fitting the signal $(1–Z)$ as a function of the delay time enables us to determine k_b directly. The method yields values of exchange rates in the cortex of the normal rat brain of $k_{b,NOE} = 17 \text{ s}^{-1}$ and $k_{b,NH} = 30 \text{ s}^{-1}$ (Xu *et al* 2013a).

Free-precession rotations by frequency-labeled exchange.   The basic idea of using the free-precession rotations as frequency-sensitive preparation was first studied in the Xenon-HyperCEST system (Garcia *et al* 2007). For protons, this frequency–labeled exchange (FLEX) was first reported by Friedman *et al* and afterwards by Yadav *et al* (Friedman *et al* 2010, Yadav *et al* 2013, 2012).

FLEX uses a broad range of rotation angles for the magnetization vectors of the different pools. Rotation is induced by a non-selective tip toward the transverse plane and by the chemical-shift-dependent accumulation of relative phases of the different pools during the evolution time. This state is then flipped back to the *z*-axis and transfer effects occur during exchange time t_{ex}. In contrast to rotation by inducing a flip angle $\theta = \gamma \ B_1 \ t_p$ via selective rf irradiation, the FLEX preparation is not frequency-selective. However, the Fourier transformation of the modulated water signal as a function of the evolution time yields a spectrum of exchanging peaks. FLEX may provide improved selectivity, because line broadening due to B_1 is avoided and faster exchanging pools can still be labeled. Tipping pulses can be very short due to non-selectivity and hence the labeling efficiency of FLEX was reported to be generally higher than the labeling efficiency of CEST (figure 17, (Yadav *et al* 2012)). This feature is of particular interest for detection of fast exchanging pools *in vivo*. Since clinical scanners supply B$_1$ amplitudes in the order of 10 μT—which corresponds to a maximum exchange rate of $k_b \sim 3000 \text{ s}^{-1}$ for CEST approaches—then fast exchanging protons can still be effectively labeled by non-selective preparation of FLEX. Until now, only slowly exchanging APT and NOE were detected *in vivo* with FLEX with similar effect and selectivity as CEST (Yadav *et al* 2013).

However, evolution in the transverse plane goes along with fast T_{2s}^* decay in contrast to the slower $T_{1\rho}$-dominated decay in CEST experiments. This additional constraint limits FLEX

to the studies of exchanging protons with $k > R_{2s}^*$. The width of the Lorentzian line obtained by the Fourier transformation of the FLEX signal decay (Yadav *et al* 2012) amounts to

$$\Gamma_{\text{FLEX}} = 2\left(k_b + \frac{1}{T_{2b}^*}\right). \tag{83}$$

For comparison, the linewidth in the case of cw-CEST with $\omega_1 = k_b$ and $\alpha = 0.5$ is given by equation (45):

$$\Gamma_{\text{CEST}} = 2\sqrt{\omega_1^2 + k_b^2} = 2\frac{1}{\sqrt{1-\alpha}}k_b \approx 2\sqrt{2}k_b. \tag{84}$$

Hence for $\alpha = 0.5$, the selectivity of FLEX and CEST is comparable, but to keep α constant with increasing k_b, B_1 must also increase in a CEST experiment.

Similar to the sampling of Z-spectrum data, sampling of FLEX data can be enhanced by increasing the maximal evolution time, while the minimal evolution time determines the spectral range (Nyquist theorem). Large chemical shifts require small dwell time Δt and small chemical shifts demand a long evolution time.

Two frequency irradiation. MTR$_{\text{SAFARI}}$, proposed by Scheidegger *et al* (2011), utilizes the intrinsic dependence of direct saturation and MT on B_1 which is assumed to be linear. An additional labeling simultaneously at two frequencies allows us to isolate CEST from spillover and MT without the need of T_1 or T_2 measurements. MTR$_{\text{SAFARI}}$ is interesting, because it is robust against B_0 inhomogeneities. However, MTR$_{\text{SAFARI}}$ is only valid if R_{ex} is in the full-saturation limit and if direct effects are linear functions of the rf power.

A detailed study of two-frequency irradiation was performed by Lee *et al* (2012). They use cosine-shaped pulses with modulation frequencies in the range of 3 to 4 kHz to create-dual frequency irradiation which is also able to eliminate asymmetric MT. This *uniform*-MT CEST is interesting for studies of tissue with a large semi-solid MT pool, e.g. cartilage (Lee *et al* 2013).

Quantitative versus fast imaging. In an ideal saturation transfer experiment, the initial state of the spin system is fully relaxed. Then, cw irradiation is performed with specific frequency and amplitude for a certain saturation time and immediately after irradiation the signal is recorded. Readout is followed by a delay time of $5 \times T_1$ before repetition. With a sequence like that transient and steady-state Z-spectra can be studied.

However, in applications of CEST to human studies a compromise must be found between short examination times and time spent for sufficient preparation of contrast. Instead of single-slice approaches, often 3D imaging is demanded. Acceleration of data acquisition can be achieved by (1) preparation of a steady-state of readout and saturation, or by (2) short transient-state saturation and fast readout. More detailed discussion of CEST imaging issues can be found in the reviews (Liu *et al* 2013b, Vinogradov *et al* 2013)

Steady-state with and without imaging elements. Steady-state-pulsed-CEST (SSP-CEST) can be acquired by two different methods. Either, the steady-state is driven by a saturation pulse train and a fast image acquisition is performed immediately afterwards, or the preparation pulses and readout are interleaved leading to a steady-state which depends on pulse train and imaging parameters (Liu *et al* 2013b). The interleaved SSP-CEST is advantageous with respect to scanning time and resolution in 3D- or multi-slice mode since the transition to the steady-state (duration $\sim T_1$) has to be done only once per offset and afterwards well prepared k-space lines can be acquired. This transition time can be saved and used to acquire outer k-space

lines—a process which does not affect the image contrast (Sled and Pike 2000, Jones *et al* 2012, 2013, Desmond and Stanisz 2012).

Transient-state approaches.   Since R_{ex} determines the decay toward steady-state (equation (18)), measurements of this rate also yield an exchange-weighted contrast and even exchange rates (equations (18), (66) and (71)) (Jin and Kim 2012, McMahon *et al* 2006, Sun 2012). Commonly the term QUEST (QUantification of Exchange by Saturation Time) is used to describe methods that employ the saturation time (see section 4.7 for theory). Recent reports show that the accuracy of rate determination in MT can be improved by the inversion of the magnetization before the pulse train (Mangia *et al* 2011). Vinogradov *et al* (2012) showed that this $T_{1\rho}$-inversion recovery approach yields a positive CEST contrast by adjusting the inversion time. For SL, this type of preparation was already employed *in vivo* by Santyr *et al* (1994) and then extended by the iSL and iTIP (toggling inversion preparation) techniques of Jin and Kim (2012). Theoretically, preceding inversion for SL can be modeled by changing the projection factor P_{zeff} to -1, in the case of CEST to $-\cos\theta$ in equation (18). In particular, the dynamic range of the reference scan can be increased by the preceding inversion.

Generally, transient approaches must start from a known initial point. This can be either a defined imaging steady-state or a partially to fully relaxed state thereafter. This is basically the same problem as for T_1 imaging where inversion or saturation recovery and more sophisticated approaches (Look and Locker 1970) reduce time of image acquisition.

Conclusion

In vivo MRZS enables a specific MR imaging contrast owing to the amplification of saturation transfer effects mediated by the water proton signal that is weighted by physiological tissue parameters. However, the evaluation and quantification of these effects is a complex problem since water pool relaxation, direct saturation and competing MT effects interfere strongly in *in vivo* systems, in particular, at the relatively low field strengths of clinical MRI systems. In addition, the saturation pulse parameters determine strength and selectivity of the CEST effects. By understanding the relation between the different effects and their dependence on crucial parameters such as metabolite concentration and exchange rates, the observed effects can be corrected, isolated and quantified. With quantitative CEST techniques, metabolite concentrations and acidity (pH) can be determined and dedicated CEST biosensor imaging become possible. This makes Z-spectroscopy an interesting tool for non-invasive studies of living tissues and pathologies with correlation on a molecular level.

Acknowledgments

References

Abergel D and Palmer A G 2004 Approximate solutions of the Bloch–McConnell equations for two-site chemical exchange *Chem. Phys. Chem.* **5** 787–93
Abergel D and Palmer A G 3rd 2005 A Markov model for relaxation and exchange in NMR spectroscopy *J. Phys. Chem.* B **109** 4837–44

Adler R S and Yeung H N 1993 Transient decay of longitudinal magnetization in heterogeneous spin systems under selective saturation: III. Solution by projection operators *J. Magn. Reson.* **104** 321–30

Aime S, Calabi L, Biondi L, De Miranda M, Ghelli S, Paleari L, Rebaudengo C and Terreno E 2005 Iopamidol: exploring the potential use of a well-established x-ray contrast agent for MRI *Magn. Reson. Med.* **53** 830–4

Aime S, Delli Castelli D and Terreno E 2002 Novel pH-reporter MRI contrast agents *Angew. Chem.* **114** 4510–2

Baguet E and Roby C 1997 Off-resonance irradiation effect in steady-state NMR saturation transfer *J. Magn. Reson.* **128** 149–60

Bar-Shir A *et al* 2013 Transforming thymidine into a magnetic resonance imaging probe for monitoring gene expression *J. Am. Chem. Soc.* **135** 1617–24

Bloch F 1946 Nuclear induction *Phys. Rev.* **70** 460

Butcher J C 1987 *The Numerical Analysis Of Ordinary Differential Equations: Runge–Kutta and General Linear Methods* (New York: Wiley-Interscience)

Cai K, Haris M, Singh A, Kogan F, Greenberg J H, Hariharan H, Detre J A and Reddy R 2012 Magnetic resonance imaging of glutamate *Nature Med.* **18** 302–6

Chan K W Y, McMahon M T, Kato Y, Liu G, Bulte J W M, Bhujwalla Z M, Artemov D and van Zijl P C M 2012 Natural D-glucose as a biodegradable MRI contrast agent for detecting cancer *Magn. Reson. Med.* **68** 1764–73

De Leon-Rodriguez L M, Lubag A J M, Malloy C R, Martinez G V, Gillies R J and Sherry A D 2009 Responsive MRI agents for sensing metabolism *in vivo Acc. Chem. Res.* **42** 948–57

Desmond K L, Moosvi F and Stanisz G J 2013 Mapping of amide, amine, and aliphatic peaks in the CEST spectra of murine xenografts at 7 T *Magn. Reson. Med.* (Early view, doi:10.1002/mrm.24822)

Desmond K L and Stanisz G J 2012 Understanding quantitative pulsed CEST in the presence of MT *Magn. Reson. Med.* **67** 979–90

Dixon W T, Hancu I, Ratnakar S J, Sherry A D, Lenkinski R E and Alsop D C 2010a A multislice gradient echo pulse sequence for CEST imaging *Magn. Reson. Med.* **63** 253–6

Dixon W T, Ren J, Lubag A J M, Ratnakar J, Vinogradov E, Hancu I, Lenkinski R E and Sherry A D 2010b A concentration-independent method to measure exchange rates in PARACEST agents *Magn. Reson. Med.* **63** 625–32

Dula A N, Arlinghaus L R, Dortch R D, Dewey B E, Whisenant J G, Ayers G D, Yankeelov T E and Smith S A 2012 Amide proton transfer imaging of the breast at 3 T: establishing reproducibility and possible feasibility assessing chemotherapy response *Magn. Reson. Med.* **70** 216–24

Englander S W, Downer N W and Teitelbaum H 1972 Hydrogen exchange *Annu. Rev. Biochem.* **41** 903–24

Forsen S and Hoffman R A 1963 Study of moderately rapid chemical exchange reactions by means of nuclear magnetic double resonance *J. Chem. Phys.* **39** 2892–901

Friedman J I, McMahon M T, Stivers J T and Van Zijl P C M 2010 Indirect detection of labile solute proton spectra via the water signal using frequency-labeled exchange (FLEX) transfer *J. Am. Chem. Soc.* **132** 1813–5

Garcia S, Chavez L, Lowery T J, Han S-I, Wemmer D E and Pines A 2007 Sensitivity enhancement by exchange mediated magnetization transfer of the xenon biosensor signal *J. Magn. Reson.* **184** 72–77

Gerigk L, Schmitt B, Stieltjes B, Röder F, Essig M, Bock M, Schlemmer H-P and Röthke M 2012 7 Tesla imaging of cerebral radiation necrosis after arteriovenous malformations treatment using amide proton transfer (APT) imaging *J. Magn. Reson. Imaging* **35** 1207–9

Grad J and Bryant R G 1990 Nuclear magnetic cross-relaxation spectroscopy *J. Magn. Reson.* **90** 1–8

Grunwald E, Jumper C F and Meiboom S 1962 Kinetics of proton transfer in methanol and the mechanism of the abnormal conductance of the hydrogen ion *J. Am. Chem. Soc.* **84** 4664–71

Haneder S, Apprich S R, Schmitt B, Michaely H J, Schoenberg S O, Friedrich K M and Trattnig S 2012 Assessment of glycosaminoglycan content in intervertebral discs using chemical exchange saturation transfer at 3.0 Tesla: preliminary results in patients with low-back pain *Eur. Radiol.* **23** 861–8

Haris M, Cai K, Singh A, Hariharan H and Reddy R 2011 *In vivo* mapping of brain myo-inositol *NeuroImage* **54** 2079–85

Haris M, Nanga R P R, Singh A, Cai K, Kogan F, Hariharan H and Reddy R 2012a Exchange rates of creatine kinase metabolites: feasibility of imaging creatine by chemical exchange saturation transfer MRI *NMR Biomed.* **25** 1305–9

Haris M, Singh A, Cai K, Nath K, Crescenzi R, Kogan F, Hariharan H and Reddy R 2013 MICEST: a potential tool for non-invasive detection of molecular changes in Alzheimer's disease *J. Neurosci. Methods* **212** 87–93

Haris M *et al* 2012b Imaging of glutamate neurotransmitter alterations in Alzheimer's disease *NMR Biomed.* **26** 386–91

Henkelman R M, Huang X, Xiang Q S, Stanisz G J, Swanson S D and Bronskill M J 1993 Quantitative interpretation of magnetization transfer *Magn. Reson. Med.* **29** 759–66

Henkelman R M, Stanisz G J and Graham S J 2001 Magnetization transfer in MRI: a review *NMR Biomed.* **14** 57–64

Hills B P, Cano C and Belton P S 1991 Proton NMR relaxation studies of aqueous polysaccharide systems *Macromolecules* **24** 2944–50

Jia G *et al* 2011 Amide proton transfer MR imaging of prostate cancer: a preliminary study *J. Magn. Reson. Imaging* **33** 647–54

Jin T, Autio J, Obata T and Kim S 2011 Spin-locking versus chemical exchange saturation transfer MRI for investigating chemical exchange process between water and labile metabolite protons *Magn. Reson. Med.* **65** 1448–60

Jin T and Kim S-G 2012 Quantitative chemical exchange sensitive MRI using irradiation with toggling inversion preparation *Magn. Reson. Med.* **68** 1056–64

Jin T and Kim S-G 2013a *In vivo* saturation transfer imaging of nuclear Overhauser effect from aromatic and aliphatic protons: implication to APT quantification *Proc. ISMRM 21st Annu. Meeting (Salt Lake City, UT)* pp 2528

Jin T and Kim S-G 2013b Off-resonance irradiation power to optimize the CEST sensitivity versus the exchange rate-specificity *Proc. ISMRM 21st Annu. Meeting (Salt Lake City, UT)* pp 2550

Jin T, Wang P, Zong X and Kim S-G 2012a Magnetic resonance imaging of the amine-proton exchange (APEX) dependent contrast *NeuroImage* **59** 1218–27

Jin T, Wang P, Zong X and Kim S-G 2012b MR imaging of the amide-proton transfer effect and the pH-insensitive nuclear Overhauser effect at 9.4 T *Magn. Reson. Med.* **69** 760–70

Jones C K, Polders D, Hua J, Zhu H, Hoogduin H J, Zhou J, Luijten P and van Zijl P C M 2012 *In vivo* three-dimensional whole-brain pulsed steady-state chemical exchange saturation transfer at 7 T *Magn. Reson. Med.* **67** 1579–89

Jones C K, Schlosser M J, van Zijl P C M, Pomper M G, Golay X and Zhou J 2006 Amide proton transfer imaging of human brain tumors at 3T *Magn. Reson. Med.* **56** 585–92

Jones C K *et al* 2013 Nuclear Overhauser enhancement (NOE) imaging in the human brain at 7 T *NeuroImage* **77** 114–24

Kim M, Gillen J, Landman B A, Zhou J and van Zijl PCM 2009 Water saturation shift referencing (WASSR) for chemical exchange saturation transfer (CEST) experiments *Magn. Reson. Med.* **61** 1441–50

Kogan F, Haris M, Singh A, Cai K, Debrosse C, Nanga R P R, Hariharan H and Reddy R 2013 Method for high-resolution imaging of creatine *in vivo* using chemical exchange saturation transfer *Magn. Reson. Med.* Early view, doi:10.1002/mrm.24641

Kreis R, Ernst T and Ross B D 1993 Absolute quantitation of water and metabolites in the human brain: II. Metabolite concentrations *J. Magn. Reson.* B **102** 9–19

Krusche-Mandl I, Schmitt B, Zak L, Apprich S, Aldrian S, Juras V, Friedrich K M, Marlovits S, Weber M and Trattnig S 2012 Long-term results 8 years after autologous osteochondral transplantation: 7 T gagCEST and sodium magnetic resonance imaging with morphological and clinical correlation *Osteoarthritis Cartilage* **20** 357–63

Lee J-S, Parasoglou P, Xia D, Jerschow A and Regatte R R 2013 Uniform magnetization transfer in chemical exchange saturation transfer magnetic resonance imaging *Sci. Rep.* **3** 1707

Lee J-S, Regatte R R and Jerschow A 2012 Isolating chemical exchange saturation transfer contrast from magnetization transfer asymmetry under two-frequency rf irradiation *J. Magn. Reson.* **215** 56–63

Li A X, Hudson R H E, Barrett J W, Jones C K, Pasternak S H and Bartha R 2008 Four-pool modeling of proton exchange processes in biological systems in the presence of MRI-paramagnetic chemical exchange saturation transfer (PARACEST) agents *Magn. Reson. Med.* **60** 1197–206

Liepinsh E and Otting G 1996 Proton exchange rates from amino acid side chains–implications for image contrast *Magn. Reson. Med.* **35** 30–42

Ling W, Regatte R R, Navon G and Jerschow A 2008 Assessment of glycosaminoglycan concentration in vivo by chemical exchange-dependent saturation transfer (gagCEST) *Proc. Natl Acad. Sci. USA* **105** 2266–70

Liu D, Zhou J, Xue R, Zuo Z, An J and Wang D J J 2013c Quantitative characterization of nuclear overhauser enhancement and amide proton transfer effects in the human brain at 7 tesla *Magn. Reson. Med.* **70** 1070–81

Liu G, Chan K W Y, Song X, Zhang J, Gilad A A, Bulte J W M, van Zijl P CM and McMahon M T 2013a Normalized Magnetization Ratio (NOMAR) filtering for creation of tissue selective contrast maps *Magn. Reson. Med.* **69** 516–23

Liu G, Gilad A A, Bulte J W M, van Zijl P C M and McMahon M T 2010 High-throughput screening of chemical exchange saturation transfer MR contrast agents *Contrast Media Mol. Imaging* **5** 162–70

Liu G, Song X, Chan K W Y and McMahon M T 2013b Nuts and bolts of chemical exchange saturation transfer MRI *NMR Biomed.* **26** 810–28

Longo D, Colombo S, Dastrù W, Poggi L, Tedoldi F, Terreno E, Uggeri F and Aime S 2009 CMR2009: 11.02: evaluating iopamidol as pH-responsive CEST agent at 3 and 7 T *Contrast Media Mol. Imaging* **4** 294–5

Longo D L *et al* 2010 Iopamidol as a responsive MRI-chemical exchange saturation transfer contrast agent for pH mapping of kidneys: In vivo studies in mice at 7 T *Magn. Reson. Med.* **65** 202–11

Look D C and Locker D R 1970 Time saving in measurement of NMR and EPR relaxation times *Rev. Sci. Instrum.* **41** 250–1

Mangia S, De Martino F, Liimatainen T, Garwood M and Michaeli S 2011 Magnetization transfer using inversion recovery during off-resonance irradiation *Magn. Reson. Imaging* **29** 1346–50

Mangia S, Liimatainen T, Garwood M and Michaeli S 2009 Rotating frame relaxation during adiabatic pulses versus conventional spin lock: simulations and experimental results at 4 T *Magn. Reson. Imaging* **27** 1074–87

McConnell H M 1958 Reaction rates by nuclear magnetic resonance *J. Chem. Phys.* **28** 430

McMahon M T, Gilad A A, Zhou J, Sun P Z, Bulte J W M and van Zijl P C M 2006 Quantifying exchange rates in chemical exchange saturation transfer agents using the saturation time and saturation power dependencies of the magnetization transfer effect on the magnetic resonance imaging signal (QUEST and QUESP): Ph calibration for poly-L-lysine and a starburst dendrimer *Magn. Reson. Med.* **55** 836–47

McVicar N, Li A X, Suchý M, Hudson R H E, Menon R S and Bartha R 2012 Simultaneous *in vivo* pH and temperature mapping using a PARACEST-MRI contrast agent *Magn. Reson. Med.* **70** 1016–25

Meldrum T, Bajaj V S, Wemmer D E and Pines A 2011 Band-selective chemical exchange saturation transfer imaging with hyperpolarized xenon-based molecular sensors *J. Magn. Reson.* **213** 14–21

Meldrum T, Schröder L, Denger P, Wemmer D E and Pines A 2010 Xenon-based molecular sensors in lipid suspensions *J. Magn. Reson.* **205** 242–6

Michaeli S, Sorce D J, Springer C S Jr, Ugurbil K and Garwood M 2006 T1ρ MRI contrast in the human brain: modulation of the longitudinal rotating frame relaxation shutter-speed during an adiabatic RF pulse *J. Magn. Reson.* **181** 135–47

Miloushev V Z and Palmer A G III 2005 R1ρ relaxation for two-site chemical exchange: general approximations and some exact solutions *J. Magn. Reson.* **177** 221–7

Morrison C and Mark Henkelman R 1995 A model for magnetization transfer in tissues *Magn. Reson. Med.* **33** 475–82

Morrison C, Stanisz G and Henkelman R M 1995 Modeling magnetization transfer for biological-like systems using a semi-solid pool with a super-Lorentzian lineshape and dipolar reservoir *J. Magn. Reson.* B **108** 103–13

Mulkern R V and Williams M L 1993 The general solution to the Bloch equation with constant rf and relaxation terms: application to saturation and slice selection *Med. Phys.* **20** 5–13

Murase K 2012 Behavior of the magnetization in spin-locking magnetic resonance imaging using numerical solutions to the time-dependent Bloch equations *Phys. Med. Biol.* **57** N481–92

Murase K and Tanki N 2011 Numerical solutions to the time-dependent Bloch equations revisited *Magn. Reson. Imaging* **29** 126–31

Neuhaus D and Williamson M 1989 *The NOE Effect in Structural and Conformational Analysis* (New York: VCH) p 164

Op 't Eijnde B, Ursø B, Richter E A, Greenhaff P L and Hespel P 2001 Effect of oral creatine supplementation on human muscle GLUT4 protein content after immobilization *Diabetes* **50** 18–23

Portnoy S and Stanisz G J 2007 Modeling pulsed magnetization transfer *Magn. Reson. Med.* **58** 144–55

Robinson T M, Sewell D A, Hultman E and Greenhaff PL 1999 Role of submaximal exercise in promoting creatine and glycogen accumulation in human skeletal muscle *J. Appl. Physiol.* **87** 598–604

Roeloffs V, Zaiss M and Bachert P 2013 An analytical approach towards pulsed-SL/CEST quantification *Proc. 21st Annu. Meeting of ISMRM (Salt Lake City, UT)* pp 2546

Santyr G E, Fairbanks E J, Kelcz F and Sorenson J A 1994 Off-resonance spin locking for MR imaging *Magn. Reson. Med.* **32** 43–51

Scheidegger R, Vinogradov E and Alsop D C 2011 Amide proton transfer imaging with improved robustness to magnetic field inhomogeneity and magnetization transfer asymmetry using Saturation with Frequency Alternating RF Irradiation (SAFARI) *Magn. Reson. Med.* **66** 1275–85

Schmitt B, Welsch G H, Zaiss M, Zbyn S, Goed S and Trattnig S 2012 T2 mapping and glycosaminoglycan-dependent chemical exchange saturation transfer (gagCEST) imaging of focal lesions in knee cartilage using 3 T MRI *20th Annu. ISMRM Scientific Meeting and Exhibition (Melbourne)* pp 0281

Schmitt B, Zaiß M, Zhou J and Bachert P 2011a Optimization of pulse train presaturation for CEST imaging in clinical scanners *Magn. Reson. Med.* **65** 1620–9

Schmitt B, Zamecnik P, Zaiss M, Rerich E, Schuster L, Bachert P and Schlemmer H P 2011c A new contrast in MR mammography by means of chemical exchange saturation transfer (CEST) imaging at 3 Tesla: preliminary results *RöFo* **183** 1030–6

Schmitt B, Zbýn S, Stelzeneder D, Jellus V, Paul D, Lauer L, Bachert P and Trattnig S 2011b Cartilage quality assessment by using glycosaminoglycan chemical exchange saturation transfer and (23)Na MR imaging at 7 T *Radiology* **260** 257–64

Schröder L, Chavez L, Meldrum T, Smith M, Lowery T J, Wemmer D E and Pines A 2008a Molekulare Steuerelemente zur temperaturempfindlichen Depolarisierung in der kernmagnetischen Resonanz *Angew. Chem.* **120** 4388–92

Schröder L, Lowery T J, Hilty C, Wemmer D E and Pines A 2006 Molecular imaging using a targeted magnetic resonance hyperpolarized biosensor *Science* **314** 446–9

Schröder L, Meldrum T, Smith M, Lowery T J, Wemmer D E and Pines A 2008b Temperature response of 129Xe depolarization transfer and its application for ultrasensitive NMR detection *Phys. Rev. Lett.* **100** 257603

Singh A, Cai K, Haris M, Hariharan H and Reddy R 2012 On B(1) inhomogeneity correction of *in vivo* human brain glutamate chemical exchange saturation transfer contrast at 7T *Magn. Reson. Med.* **69** 818–24

Singh A, Haris M, Cai K, Kassey V B, Kogan F, Reddy D, Hariharan H and Reddy R 2011 Chemical exchange saturation transfer magnetic resonance imaging of human knee cartilage at 3 T and 7 T *Magn. Reson. Med.* **68** 588–94

Sled J G and Pike G B 2000 Quantitative interpretation of magnetization transfer in spoiled gradient echo MRI sequences *J. Magn. Reson.* **145** 24–36

Sloniec J, Schnurr M, Witte C, Resch-Genger U, Schröder L and Hennig A 2013 Biomembrane interactions of functionalized cryptophane-A: combined fluorescence and (129) Xe NMR studies of a bimodal contrast agent *Chemistry* **19** 3110–8

Smith S A, Bulte J W M and van Zijl P C M 2009 Direct saturation MRI: theory and application to imaging brain iron *Magn. Reson. Med.* **62** 384–93

Solomon I 1955 Relaxation processes in a system of two spins *Phys. Rev.* **99** 559

Spence M M, Rubin S M, Dimitrov I E, Ruiz E J, Wemmer D E, Pines A, Yao S Q, Tian F and Schultz P G 2001 Functionalized xenon as a biosensor *Proc. Natl Acad. Sci.* **98** 10654–7

Stanisz G J, Odrobina E E, Pun J, Escaravage M, Graham S J, Bronskill M J and Henkelman R M 2005 T1, T2 relaxation and magnetization transfer in tissue at 3T *Magn. Reson. Med.* **54** 507–12

Steenge G R, Lambourne J, Casey A, Macdonald I A and Greenhaff P L 1998 Stimulatory effect of insulin on creatine accumulation in human skeletal muscle *Am. J. Physiol.* **275** E974–9

Stevens T K, Palaniappan K K, Ramirez R M, Francis M B, Wemmer D E and Pines A 2012 HyperCEST detection of a 129Xe-based contrast agent composed of cryptophane-A molecular cages on a bacteriophage scaffold *Magn. Reson. Med.* **69** 1245–52

Sun P Z 2012 Simplified quantification of labile proton concentration-weighted chemical exchange rate (k(ws)) with RF saturation time dependent ratiometric analysis (QUESTRA): normalization of relaxation and RF irradiation spillover effects for improved quantitative chemical exchange saturation transfer (CEST) MRI *Magn. Reson. Med.* **67** 936–42

Sun P Z, Farrar C T and Sorensen A G 2007a Correction for artifacts induced by B(0) and B(1) field inhomogeneities in pH-sensitive chemical exchange saturation transfer (CEST) imaging *Magn. Reson. Med.* **58** 1207–15

Sun P Z, Murata Y, Lu J, Wang X, Lo E H and Sorensen A G 2008 Relaxation-compensated fast multislice amide proton transfer (APT) imaging of acute ischemic stroke *Magn. Reson. Med.* **59** 1175–82

Sun P Z and Sorensen A G 2008 Imaging pH using the chemical exchange saturation transfer (CEST) MRI: Correction of concomitant RF irradiation effects to quantify CEST MRI for chemical exchange rate and pH *Magn. Reson. Med.* **60** 390–7

Sun P Z, van Zijl P C M and Zhou J 2005a Optimization of the irradiation power in chemical exchange dependent saturation transfer experiments *J. Magn. Reson.* **175** 193–200

Sun P Z, Wang E, Cheung J S, Zhang X, Benner T and Sorensen A G 2011 Simulation and optimization of pulsed radio frequency irradiation scheme for chemical exchange saturation transfer (CEST) MRI-demonstration of pH-weighted pulsed-amide proton CEST MRI in an animal model of acute cerebral ischemia *Magn. Reson. Med.* **66** 1042–8

Sun P Z, Zhou J, Huang J and van Zijl P 2007b Simplified quantitative description of amide proton transfer (APT) imaging during acute ischemia *Magn. Reson. Med.* **57** 405–10

Sun P Z, Zhou J, Sun W, Huang J and Zijl van P C M 2005b Suppression of lipid artifacts in amide proton transfer imaging *Magn. Reson. Med.* **54** 222–5

Tee Y K, Khrapitchev A A, Sibson N R, Payne S J and Chappell M A 2012 Evaluating the use of a continuous approximation for model-based quantification of pulsed chemical exchange saturation transfer (CEST) *J. Magn. Reson.* **222** 88–95

Terreno E, Barge A, Beltrami L, Cravotto G, Castelli D D, Fedeli F, Jebasingh B and Aime S 2008 Highly shifted LIPOCEST agents based on the encapsulation of neutral polynuclear paramagnetic shift reagents *Chem. Commun.* **7** 600–2

Terreno E, Cabella C, Carrera C, Delli Castelli D, Mazzon R, Rollet S, Stancanello J, Visigalli M and Aime S 2007 From spherical to osmotically shrunken paramagnetic liposomes: an improved generation of LIPOCEST MRI agents with highly shifted water protons *Angew. Chem., Int. Edn Engl.* **46** 966–8

Terreno E, Castelli D D and Aime S 2010 Encoding the frequency dependence in MRI contrast media: the emerging class of CEST agents *Contrast Media Mol. Imaging* **5** 78–98

Togao O, Takashi Y, Jochen K, Akio H, Koji Y, Kazufumi K, Yuriko S, Koji S, Masaya Takahashi and Hiroshi H 2012 Effect of saturation pulse length on parallel transmission based amide proton transfer (APT) imaging of different brain tumor types *Proc. 20th Annu. Meeting of ISMRM (Melbourne)* pp 0743

Trott O, Abergel D and Palmer A G 2003 An average-magnetization analysis of R 1ρ relaxation outside of the fast exchange limit *Mol. Phys.* **101** 753–63

Trott O and Palmer A G 2002 R1[ρ] relaxation outside of the fast-exchange limit *J. Magn. Reson.* **154** 157–60

Trott O and Palmer A G 3rd 2004 Theoretical study of R(1ρ) rotating-frame and R2 free-precession relaxation in the presence of *n*-site chemical exchange *J. Magn. Reson.* **170** 104–12

Van Zijl P C M and Yadav N N 2011 Chemical exchange saturation transfer (CEST): What is in a name and what isn't? *Magn. Reson. Med.* **65** 927–48

Van Zijl P C M, Zhou J, Mori N, Payen J-F, Wilson D and Mori S 2003 Mechanism of magnetization transfer during on-resonance water saturation. A new approach to detect mobile proteins, peptides, and lipids *Magn. Reson. Med.* **49** 440–9

Vinogradov E, Sherry A D and Lenkinski R E 2013 CEST: from basic principles to applications, challenges and opportunities *J. Magn. Reson.* **229** 155–72

Vinogradov E, Soesbe T C, Balschi J A, Sherry A D and Lenkinski R E 2012 pCEST: positive contrast using chemical exchange saturation transfer *J. Magn. Reson.* **215** 64–73

Ward K, Aletras A and Balaban R 2000 A new class of contrast agents for MRI based on proton chemical exchange dependent saturation transfer (CEST) *J. Magn. Reson.* **143** 79–87

Woessner D E, Zhang S, Merritt M E and Sherry A D 2005 Numerical solution of the Bloch equations provides insights into the optimum design of PARACEST agents for MRI *Magn. Reson. Med.* **53** 790–9

Wolff S D and Balaban R S 1990 NMR imaging of labile proton exchange *J. Magn. Reson.* **86** 164–9

Woods M, Woessner D E and Sherry A D 2006 Paramagnetic lanthanide complexes as PARACEST agents for medical imaging *Chem. Soc. Rev.* **35** 500–11

Wu R, Liu C-M, Liu P K and Sun P Z 2012 Improved measurement of labile proton concentration-weighted chemical exchange rate (k(ws)) with experimental factor-compensated and T(1)-normalized quantitative chemical exchange saturation transfer (CEST) MRI *Contrast Media Mol. Imaging* **7** 384–9

Xu J, Yadav N N, Bar-Shir A, Jones C K, Chan K W Y, Zhang J, Walczak P, McMahon M T and van Zijl P C M 2013a Variable delay multi-pulse train for fast chemical exchange saturation transfer and relayed-nuclear overhauser enhancement MRI *Magn. Reson. Med.* (Early view, doi:10.1002/mrm.24850)

Xu X, Lee J-S and Jerschow A 2013b Ultrafast scanning of exchangeable sites by NMR spectroscopy *Angew. Chem. Int. Edn Engl.* **52** 8281–4

Yadav N N, Jones C K, Hua J, Xu J and van Zijl P C M 2013 Imaging of endogenous exchangeable proton signals in the human brain using frequency labeled exchange transfer imaging *Magn. Reson. Med.* **69** 966–73

Yadav N N, Jones C K, Xu J, Bar-Shir A, Gilad A A, McMahon M T and van Zijl P C M 2012 Detection of rapidly exchanging compounds using on-resonance frequency-labeled exchange (FLEX) transfer *Magn. Reson. Med.* **68** 1048–55

Yeung H N, Adler R S and Swanson S D 1994 Transient decay of longitudinal magnetization in heterogeneous spin systems under selective saturation: IV. Reformulation of the spin-bath-model equations by the Redfield–Provotorov theory *J. Magn. Reson.* **106** 37–45

Yeung H N and Swanson S D 1992 Transient decay of longitudinal magnetization in heterogeneous spin systems under selective saturation *J. Magn. Reson.* **99** 466–79

Yuan J, Zhou J, Ahuja A T and Wang Y-X J 2012 MR chemical exchange imaging with spin-lock technique (CESL): a theoretical analysis of the Z-spectrum using a two-pool R(1ρ) relaxation model beyond the fast-exchange limit *Phys. Med. Biol.* **57** 8185–200

Zaiss M and Bachert P 2012a Exchange-dependent relaxation in the rotating frame for slow and intermediate exchange—modeling off-resonant spin-lock and chemical exchange saturation transfer *NMR Biomed.* **26** 507–18

Zaiss M and Bachert P 2012b Equivalence of spin-lock and magnetization transfer NMR experiments arXiv:1203.2067v1

Zaiss M, Xu J, Goerke S, Khan I S, Singer R J, Gore J C, Gochberg D F and Bachert P 2013a Inverse Z-spectrum analysis for MT- and spillover-corrected and T1-compensated steady-state pulsed CEST-MRI-application to pH-weighted MRI of acute stroke arXiv:1302.6605v2

Zaiss M, Kunz P, Goerke S, Radbruch A and Bachert P 2013b MR imaging of protein folding *in vitro* employing Nuclear-Overhauser-mediated saturation transfer *NMR Biomed.* (Early view, doi:10.1002/nbm.3021)

Zaiss M, Schmitt B and Bachert P 2011 Quantitative separation of CEST effect from magnetization transfer and spillover effects by Lorentzian-line-fit analysis of z-spectra *J. Magn. Reson.* **211** 149–55

Zaiss M, Schnurr M and Bachert P 2012 Analytical solution for the depolarization of hyperpolarized nuclei by chemical exchange saturation transfer between free and encapsulated xenon (HyperCEST) *J. Chem. Phys.* **136** 144106

Zhang S, Merritt M, Woessner D E, Lenkinski R E and Sherry A D 2003 PARACEST agents: modulating MRI contrast via water proton exchange *Acc. Chem. Res.* **36** 783–90

Zhang S, Winter P, Wu K and Sherry A D 2001 A novel europium(III)-based MRI contrast agent *J. Am. Chem. Soc.* **123** 1517–8

Zhao J M, Har-el Y, McMahon M T, Zhou J, Sherry A D, Sgouros G, Bulte J W M and van Zijl P C M 2008 Size-induced enhancement of chemical exchange saturation transfer (CEST) contrast in liposomes *J. Am. Chem. Soc.* **130** 5178–84

Zhou J 2011 Amide proton transfer imaging of the human brain *Methods Mol. Biol.* **711** 227–37

Zhou J, Payen J-F, Wilson D A, Traystman R J and van Zijl P C M 2003 Using the amide proton signals of intracellular proteins and peptides to detect pH effects in MRI *Nature Med.* **9** 1085–90

Zhou J and van Zijl P C M 2006 Chemical exchange saturation transfer imaging and spectroscopy *Prog. Nucl. Magn. Reson. Spectrosc.* **48** 109–36

Zhou J, Wilson D A, Sun P Z, Klaus J A and van Zijl P C M 2004 Quantitative description of proton exchange processes between water and endogenous and exogenous agents for WEX, CEST, and APT experiments *Magn. Reson. Med.* **51** 945–52

Zhou J, Yan K and Zhu H 2012 A simple model for understanding the origin of the amide proton transfer MRI signal in tissue *Appl. Magn. Reson.* **42** 393–402

Zhou J *et al* 2011 Differentiation between glioma and radiation necrosis using molecular magnetic resonance imaging of endogenous proteins and peptides *Nature Med.* **17** 130–4

Zu Z, Janve V A, Li K, Does M D, Gore J C and Gochberg D F 2011a Multi-angle ratiometric approach to measure chemical exchange in amide proton transfer imaging *Magn. Reson. Med.* **68** 711–9

Zu Z, Janve V A, Xu J, Does M D, Gore J C and Gochberg D F 2012 A new method for detecting exchanging amide protons using chemical exchange rotation transfer *Magn. Reson. Med.* **69** 637–47

Zu Z, Li K, Janve V A, Does M D and Gochberg D F 2011b Optimizing pulsed-chemical exchange saturation transfer imaging sequences *Magn. Reson. Med.* **66** 1100–8